Sorption of PFAS onto synthetic hydrous iron oxides

An experimental approach

Sigbjørn Økland

Thesis submitted for the degree of
Master of Science in Environmental Geoscience
60 credits

Department of Geoscience
Faculty of Mathematics and Natural Sciences

UNIVERSITY OF OSLO

October, 2020

Sorption of PFAS onto synthetic hydrous iron oxides

An experimental approach

Sigbjørn Økland

Sorption of PFAS onto synthetic hydrous iron oxides

Abstract

Perfluorinated alkyl substances (PFAS) are organic compounds developed in the 1940s with a large variety of properties that are used in numerous industrial and commercial applications. Perfluorinated carboxylic acids (PFCAs), a subgroup of PFAS, are of growing concern as many of them are toxic to humans and can be transported over long distances. Determining transport and mapping distribution between various environmental compartments is an important step in assessing the full impact of PFAS contamination. Most research on PFAS sorption to soil focus on sorption to organic carbon. Some studies have found that PFOS will also sorb to positively charged iron oxides like goethite and hematite in the soil. Here it is suggested that PFAS effectively sorbs to 2-line ferrihydrite (Fh), a common nanoparticulate iron oxyhydroxide mineral in soils.

Experimental batch reactions with synthetic Fh and four PFCAs (C5, C8, C9, C10) were carried out along concentration gradients. Sorption samples were measured with ATR-FTIR, and some additional samples for PFOA and PFDA were studied with LC-MS/MS. Sorption isotherms were drawn based on IR absorbance of the PFCAs on Fh. The sorption fits well with a non-linear ($n < 1$) Freundlich isotherm for all PFCAs. The Freundlich equilibrium, K_f, for PFPeA, PFOA, PFNA and PFDA was 5.9 ($n = 0.32$), 8.5 ($n = 0.51$), 579 ($n = 0.85$), and 128 ($n = 0.79$), respectively. These were used to make a transport model with the geochemical tool PHREEQC. The characteristics of the Gardermoen unconfined aquifer were chosen for the simulation due to a pollution history in the area with PFAS in aqueous film-forming foams from a fire-fighting practice facility. Spectral analyses of sorption samples indicate that PFCAs sorb by inner sphere ligand exchange on the Fh surface. The transport model predicts chain length dependent sorption of PFCAs to Fh, where longer chained PFCAs (C9, C10) have higher retardation factors than shorter chained PFCAs (C5, C8). LC-MS/MS results of PFOA and PFDA strengthened interpretations of chain length dependent sorption. This thesis is the first to explore sorption of PFCAs to ferrihydrite and contributes to the knowledge of PFAS transport in the soil environment.

II

Acknowledgements

Table of Contents

1. Introduction

1.1 Contaminants in the environment

Studying the mechanisms and interactions of soil biogeochemistry is important to understand the fate of contaminants in the environment and the extent of their negative effects. Vast and increasing amounts of toxicants have been deposited into soil, water and air since the industrialization (Komatina, 2004). Increased knowledge on contaminants' environmental effects is the first step in creating preventative legislation to control the production and release of toxicants. Contaminants are often discovered and classified as toxic after deposition has been going on for years, as is the case with the substances of interest in this thesis. Whenever a contaminant has been classified as toxic there usually remains a lot of work to be done in terms of understanding the substances' total environmental impact. This is exacerbated by the fact that there are estimates of several hundred potential persistent organic pollutants (POPs) that have not yet been evaluated (Scheringer et al., 2012). Many contaminants have very long half-lives (Ashraf, 2017; Scheringer et al., 2012), making it all the more relevant to study their effects even long after the most intense periods of production and utilization.

1.2 History of PFAS production and use

Poly- and perfluoroalkyl substances (PFAS) were invented in the 1930s, and electrochemical fluorination, the first industry method of PFAS production, was licensed in the 1940s by 3M (Banks et al., 1994). PFAS were sought because of their use as surface-active agents (abbr. surfactant), being both lipo- and hydrophobic they were ideal for many industrial appliances. Gradually, they were produced for commercial purposes and have been used in numerous consumer products since, including: non-stick cookware, waterproof fabrics, firefighting foams, protective coatings, food packaging, ski waxes and many more (3M, 1999; Kissa, 2001). They are usually produced through electrochemical fluorination or telomerization (Buck et al., 2011). The use of certain PFAS and their degradation products were not banned in the EU until relatively recently. POPs are defined as substances which are highly persistent, transported over long distances, distributed in environmental compartments including soil, water and air, bioaccumulative as well as biomagnified and are toxic to humans and other biota (Secretariat of the Stockholm Convention (SSC), 2018). In 2006, legislation passed deciding EU would follow the commitments by the Stockholm convention (European Union, 2006). The Stockholm convention, responsible for the registration of POPs, put out international bans for PFOS and PFOA in 2009 and 2019, respectively (Stockholm Convention, 2009; Stockholm Convention, 2019). There are increased concentrations of PFAS in snow tracks used for testing skis and ski wax (Norwegian Institute for Air Research, 2019) and subsequently, the use of ski wax was banned from use by the International Ski Federation (Fédération Internationale de Ski or FIS) from 2020 (International Ski Federation, 2019). How PFAS and adjacent substances sorb to soil minerals is a valuable step in furthering the knowledge on the extent and effect of historical pollution.

1.3 Soil processes and stratification

Podzolic soils (figure 1) are the most common soil type in boreal forests, which covers 37.4% of the Norwegian mainland (Statistics Norway (SSB), 2019). In podzolic soils, the upper layers (O and A horizon) are very rich in organic matter (OM) and their decomposition products (humus). Organic acids together with the surface soil being in atmospheric equilibrium with CO_2, gives a lower pH of around 4 - 5.5. Water infiltration down the soil column transports organic acids and cation complexes from the low pH zone and leaves behind a leached, ashen grey layer (E horizon). With further depth the pH is raised and cations precipitate as minerals, primarily hydrous iron- and aluminum oxides together with some OM (B horizon). This layer is thereby characterized by the color of the iron oxides with a deep brown/red color in contrast to the overlaying leached layer. (vanLoon and Duffy, 2017)
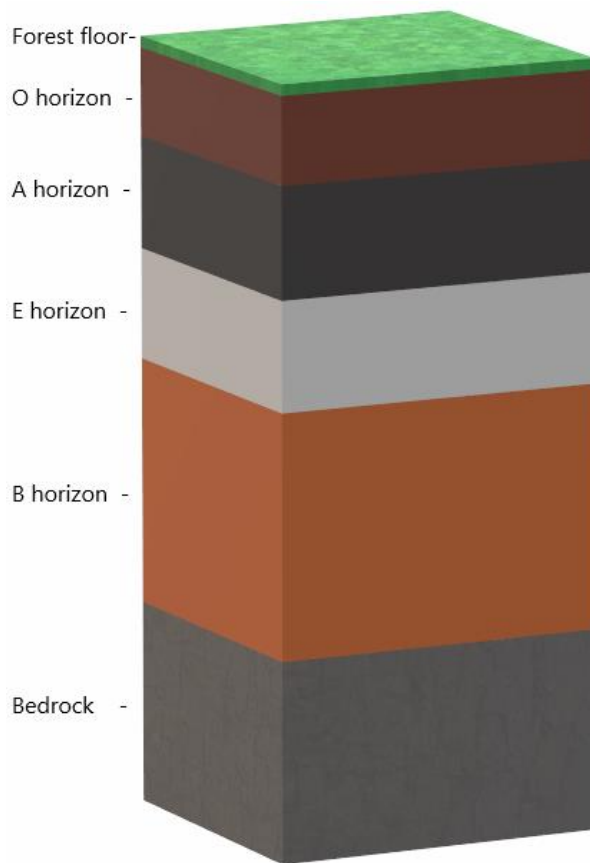
Figure 1: Basic illustration of what a podzolic stratification of the soil might look like. Depth of profile and relative thicknesses of layers can vary.

1.4 Iron oxides, their properties and role in the environment

Iron oxides and hydroxides are important in soil chemistry because of their large surface area, small particle size, high porosity and variable surface charge leading to their high reactivity and sorption capacity. Freshly formed 2-line Ferrihydrite (hereafter Fh) particles have an estimated average diameter of 2.6 nm, can have a surface area of up to 650 m^2/g and a mass density of 3.5 g/cm^3 (Hiemstra and Van Riemsdijk, 2009). There will of course be variations in these values as synthetization processes of Fh may differ, but they provide an understanding of the magnitude of iron oxide properties. There are several naturally occurring iron oxide minerals in soils e.g. hematite (Fe_2O_3), goethite (FeO(OH)) and ferrihydrite (Fe_2O_3 * 0.5 H_2O, one of many proposed stoichiometries) being the most common. In the B horizon of boreal podzol soils there are enriched amounts of sesquioxides, which include all minerals on the form X_2O_3, where X is usually a trivalent metal cation e.g. Al^{3+} and Fe^{3+}. A significant amount of these are iron oxides due to the podzolization process that was briefly described in the last section. Fh has a point of zero net proton charge of around pH 7.9-8.7 (Villalobos and Antelo, 2011), meaning it will have positive surface charge at lower pH. Iron oxides' sorptive properties are well understood for many adsorbates, but there have been calls for studies on the effect iron oxides have on perfluorinated compound (PFC) sorption (Enevoldsen and Juhler, 2010; Wei et al., 2017).

1.5 Per- and polyfluoroalkyl substances (PFAS)

PFAS are alkyl substances in which the hydrogen atoms have been replaced by fluoride to give them the desired properties. If all hydrogen atoms are replaced by fluorine, they are perfluorinated, and if only some have been replaced they are polyfluorinated. In this thesis, only the perfluorinated compounds will be discussed. The C-F bond has a higher bond enthalpy than C-H because a covalent C-F bond has a higher difference in electronegativity than C-H, making it highly polar and giving the bond an ionic character (Hagan, 2008). Furthermore, for every fluorine atom bound to the same carbon atom there is an increase in bond strengths of all geminal C-F bonds as carbon becomes increasingly positively charged (Wiberg and Rablen, 1993). There is usually a functional group, e.g. a carboxyl or a sulphonate group, at the end of the carbon chain, causing them to be anionic when dissociating in water. The functional group (head) is hydrophilic and the rest of the C-F-chain (tail) is hydrophobic. Perfluorinated n-alkanes do not exhibit the same straight zig zag shape as their hydrocarbon counterparts, but twists into a helical shape, likely due to hyperconjugation (Cormanich et al., 2017), but electrostatic repulsion (Jang et al., 2003) as well as steric repulsion (Bunn and Howells, 1954) has also been suggested. This shape allows fluorine to better cover the carbon skeleton and contributes to their persistence (Siegemund et al., 2000). PFAS are chemically resistant and can withstand elevated temperatures (Kunieda and Shinoda, 1976) making them highly versatile as surfactants. The properties of PFAS which makes them so versatile are also what make them very persistent with a low degradability.

This thesis will examine four different perfluorinated carboxylic acids (PFCAs) over a range of carbon chain lengths; perfluorinated pentanoic acid (PFPeA, C5), perfluorinated octanoic acid (PFOA, C8), perfluorinated nonanoic acid (PFNA, C9) and perfluorinated decanoic acid (PFDA, C10). PFOA together with perfluorooctane sulphonate (PFOS), are the most studied PFAS in terms of health and environmental effects, as they are common degradation products of PFCs (ATSDR, 2018; UNEP, 2006).

1.6 Review of PFAS sorption to soil matter and the methods used

Where sorption isotherms have been constructed for PFAS on soils, they have best been described by the Freundlich model (Enevoldsen and Juhler, 2010; Wei et al., 2017; Higgins and Luthy, 2006). A major controlling parameter for sorption of PFAS is pH (Gao and Chorover, 2012; Higgins and Luthy, 2006; Johnson et al., 2007; Enevoldsen and Juhler, 2010), where they observe increased sorption with decreasing pH. Higgins and Luthy (2006) deems it likely that pH mostly affects the sorbents, as pH would have the most effect on the PFAS when it gets close to their pKa's, which are relatively low (<3.8) for most PFCAs and even lower for their sulphonate counterparts. The pKa values of PFCAs are highly debated. PFOA alone have reported pKa's in a range of $0 - 3.8$, while PFPeA, PFNA and PFDA have pKa's of 0.569, 2.575 and 2.606, respectively (Ding and Peijnenburg, 2013, and references therein). The highest pKa of PFOA at 3.8 has been criticized as being an overestimation due to the use of methanol-water mixture as a solvent, thus not achieving a true pure water pKa (Kutsuna et al., 2012). PFCAs will have higher experimental pKa when solvated in 50%

methanol as it suppresses effects of aggregation and stabilizes undissociated PFCAs (Cabala et al., 2017; Kutsuna et al., 2012).

There is a large increase of the soil-water distribution coefficient, K_d, for each additional CF_2-moiety, as well as a higher K_d for the perfluorinated sulphonic acids compared to perfluorinated carboxylic acids of equal chain length (Higgins and Luthy, 2006). It was hypothesized that this might be due to the larger size of the sulphonate group vs. the carboxylate group, causing the sulphonates to have a higher hydrophobicity. Enevoldsen and Juhler (2010) found that PFAS with shorter chain length (C<8) were only found in pore water, whereas PFAS with longer chain length (C>10) were only found in sediments.

Sorption kinetics of PFOA and PFOS onto hematite has been studied by Gao and Chorover (2012) which found that sorption rates were highly dependent on pH and surface loading. Lower pH and higher initial concentrations of PFAS gave higher rates of sorption. Wei et al. (2017) carried out batch reaction experiments of PFOS onto different soils to study sorption kinetics and found that the main rate-limiting factor was film diffusion and intraparticle diffusion.

Gao and Chorover (2012) found that PFOA sorbs to hematite through ligand exchange (inner sphere sorption), but that an increase in ionic strength causes a decrease in overall sorption, which was ascribed to electrostatic effects (outer sphere sorption) i.e. competitive sorption of ions. For PFOS they only observed electrostatic sorption and no ligand exchange.

Higgins and Luthy (2006) studied sorption controlling parameters of PFAS in sediments with organic carbon and looked at the effect of adding cations into solution. By the addition of Ca^{2+} there was a significant increase in the sorption of PFAS, but they saw no such increase in sorption with Na^+, suggesting that ionic strength is not a sole factor. They saw the effects of Ca^{2+} as a reduction in the charge of functional sites on dissolved organic matter (DOM) in the sediment, but sodium would not have the same effect as a monovalent cation. Lu et al. (2016) found co-adsorption of PFOS with Cu^{2+} and Pb^{3+}, where the presence of the heavy cations, particularly with Cu^{2+}, enhanced the sorption of PFOS. It was hypothesized that this was a result of a bridging and bilayer effect, where sorbed copper would act as a bridge for PFOS. They concede that micelles were probably not forming in their study due to the low PFOS concentrations, but that the bilayer structure might form on partial sites of the particles.

The critical micelle concentration (CMC), the concentration at which any additional surfactant will form micelles, for PFOS and PFOA is 4573 mg/l and 15696 mg/l, respectively (Kissa, 2001). Simister et al. (1992) found that ammonium perfluorooctanoate forms cylindrical micelles at the CMC. However, La Mesa and Sesta (1987) found that sodium and lithium perfluorononanoates produce few and small micellar aggregates due to the low contribution to the hydrophobic effect of the interaction between CF_2-moieties. Johnson et al. (2007) looked at the possibility that PFOS would form hemi-micelles on the sorbents which should produce a sudden increase on the sorption isotherm around the CMC, and would only require the concentration of PFAS to be 0.01-0.001 of the CMC. They did not find any clear evidence that hemi-micelles were forming, but the sorption isotherm showed a slight upward curvature for PFOS for a high iron content sand. Most sorption studies conclude that hemi-

micelles of PFAS are probably not forming, and if they are forming, they are low in numbers at environmentally relevant concentrations (Higgins and Luthy, 2006; Lu et al., 2016; Johnson et al., 2007).

Organic matter is a major controlling parameter in the sorption of PFCs in the soil (Johnson et al., 2007; Higgins and Luthy, 2006; Wei et al., 2017). While Johnson et al. (2007) found that PFOS sorb to organic carbon, the organic carbon-water distribution coefficient, K_{OC}, for all sediments studied, did not change much over a wide range of OC content (f_{OC} range: 0.03 - 0.4). They also found significant amounts of sorption in soils with no measurable OC present which led them to the conclusion that both inorganic and organic materials play a significant role in the fate and transport of PFOS in soils. Wei et al. (2017) found a positive correlation between sorption capacity of PFOS vs. aluminum and iron oxide soil content and soil organic matter.

Some methods used for sorption experiments of PFAS include: Solid Phase Extraction Liquid Chromatography Tandem Mass Spectrometry (SPE-LC-MS/MS) (Enevoldsen and Juhler, 2010), flow-through cell with Attenuated Total Reflectance – Fourier Transform Infrared spectroscopy (ATR-FTIR) (Gao and Chorover, 2012), and even Gas Chromatography-Mass Spectrometry (GC-MS) for some shorter chain (C2-C6) PFCs (Scott et al., 2006). ATR-FTIR will be the main method for measuring PFCA content in this thesis, but some supplemental data from SPE-LC-/MS/MS will be used as well. The SPE-LC-MS/MS method is often used for environmental studies on PFCs, because of its low limits of detection (LOD). For this method, Enevoldsen and Juhler (2010) reported LODs from 2 – 8 ng/l for different PFAS, and compared to the drinking water limit proposed by the European Drinking Water Directive for the grouped concentrations of all PFAS at 0.5 µg/l (European Environment Agency, 2019), the LOD of the SPE-LC-MS/MS method should be sufficient for environmental studies.

The dominating factors in the fate of PFCAs are transport to deep ocean and sediment burial. PFCAs have been discovered in atmospheric, aquatic and soil environments as well as in arctic biota. (Prevedouros et al., 2006).

For a while there was no observed biodegradation of *perfluorinated* compounds (Liu and Mejia Avendaño, 2013). The situation has been compared to organochlorines which were considered catabolically non-degradable decades ago, but microbes have since been observed to degrade them at anaerobic conditions (Parsons et al., 2008). A rationale proposed by Parsons et al. (2008) was that reductive defluorination is thermodynamically favorable (energy-yielding) and could in theory provide energy for the growth of microbes, but it was concluded that no observed microbes possess the collection of enzymes required to catalyze them through metabolic pathways (Vargas et al., 2000). A study conducted by Huang and Jaffé (2019) has now found that the bacteria *Acidimicrobium* sp. Strain A6 is able to both defluorinate and produce shorter chain fluorinated compounds, i.e. break both C-F and C-C bonds.

There is a large range of reported values for K_d and K_{OC} of PFAS to different materials, some of which are compiled in table 1.

Table 1: Distribution coefficients of certain PFAS to different materials and soils.

PFC	Sorbent	Sorption parameter	
PFPeA	Soil[a]	K_{OC}	23.4
PFOA	GAC[b]	K_f	82.14, n = 0.71
	Soil[c,g]	K_d	1.8 - 38
	Soild[a,c,f,g]	K_{OC}	4.3 - 251
PFNA	Soil[c]	K_d	7.7
	Soil[a,c,d]	K_{OC}	18 - 245
PFDA	Soil[c]	K_d	33
	Soil[a,c,d]	K_{OC}	79 - 912
PFOS	Soil[e]	K_d	63

[a]Batch reactions with various soils (Guelfo and Higgins, 2013).
[b]K_f of granular activated carbon (Zhang et al., 2019).
[c]Soil with 8.1 g Fe/kg soil (Enevoldsen and Juhler, 2010).
[d]Average of different soils (Higgins and Luthy, 2006).
[e]Ferrosol with ~81 g Fe/kg soil (Wei et al., 2017).
[f]Three sediment types with varying OC content (Ahrens et al., 2011).
[g]Six soils with varying OC content (Milinovic et al., 2015).

1.7 Brief review of health risks and toxicology of PFAS

Human exposure to PFOS/PFOA is mostly through ingestion of food or water (Fromme et al., 2009) or inhalation of dust or aerosols (ATSDR, 2018). PFOS and PFOA have been detected in both human breastmilk and blood (Kannan et al., 2004), have not been shown to metabolize and can only be removed through excretory pathways (Stahl et al., 2011). Significantly higher concentrations of PFOS has been found in liver tissue than in muscle of wild boar (Stahl et al., 2012). PFCAs (C > 7) bioconcentrate (Martin et al., 2003), bioaccumulate (Conder et al., 2008) and biomagnify (Müller et al., 2011; Kannan et al., 2004). Animal studies with PFOA has shown moderate acute toxicity through ingestion (PHE, 2009), as well as chronic toxicity with developmental effects in mice (Lau et al., 2006) and reproductive effects in rats (from ammonium PFO) (Butenhoff et al., 2004) and mice (Lau et al., 2006).

1.8 Aims of the thesis

The main aim of this thesis was to experimentally describe sorption mechanisms of PFCAs to Fh and contribute to a database for geochemical modeling. By using ATR-FTIR to study the sorption of PFCAs to synthetic Fh, the goal was to draw sorption isotherms for input into geochemical modeling tools which can be utilized to simulate environmental contamination. The use of such a model is demonstrated. Results from liquid chromatography to measure both sorbed and aqueous phase PFCAs are complementary to the FTIR results and a comparison is presented.

2. Methods

2.1 Synthesis of 2-line ferrihydrite

The synthesis of 2-line Fh followed the procedure of Schwertmann (1991). A 1 L solution of 0.1 M $Fe(NO_3)_3$ was prepared by dissolving 40.4 g $Fe(NO_3)_3*9H2O$ in 1 liter of milli-Q water. The 0.1 M $Fe(NO_3)_3$ solution was transferred to smaller beakers, continuously stirred and rapidly titrated with 1 M NaOH to reach a pH of around 7-7.5 to precipitate Fh ($Fe_2O_3*0.5H_2O$). When precipitating, a dark brown suspension was observed. In order to prevent particle growth, the solution was rapidly titrated. The suspended Fh was washed by centrifuging, removing the supernatant fluid and rinsing with milli-Q water. This process was repeated a number of times until the washing showed little effect on the specific conductance. The specific conductance after washing was just over 40 µS/cm. The Fh was freeze dried to remove the water in the samples without baking to minimize crystal growth.

2.2 X-Ray Powder Diffraction (XRPD) of ferrihydrite

XRD is a common method for determining crystal lattices in minerals. By heating up a filament (cathode) and applying a large voltage between the cathode and anode, electrons will move at great speed toward the target anode and excite the atoms. When the atoms in the target anode stabilize from the excited state, they emit electromagnetic waves in the X-ray spectrum. The choice of anode determines the energy of the emitted X-rays. (Bunaciu et al., 2015)

The rays are pointed at a varying incident angle towards a crystalline substance. XRD studies the interference patterns produced by scattering of mineral lattices. At certain angles the conditions for Bragg's law ($n\lambda = 2d\sin\theta$) are met and the rays produce constructive interference. The Bragg equation relates the wavelength (λ) of a ray to the incident angle (θ) and the length between crystal lattices (d-spacing). It specifically states that when the incident angle is such that the extra distance the photon has to travel between two crystal lattice planes ($2d\sin\theta$) is equal to the wavelength of the incoming photon, or an integer of that wavelength, there will be constructive interference.

The Fh sample was already in disaggregated form, and there should be no preferred orientation of the particles. The sample powder was packed into the sample holder disc and mounted in the diffractometer at the XRD-laboratory at the Department of Geosciences, UiO. XRPD analyses were done with a Bruker D8 ADVANCE, with a DaVinci design and a Lynxeye detector, using a copper anode as the X-ray source. A voltage of 40 kV and a current of 40 mA was applied. No monochromator was used. The diffractogram was collected in an angular range of 10°-90°, at a rate of 0.016° min^{-1} and a step count time of 3s $step^{-1}$. The sample disc was also continuously rotated during the test which should randomize potential preferred orientations.

The diffractograms are presented as 2θ vs. intensity (or number of counts). Every mineral will have a specific inner crystal structure and d-spacing. Peaks in the diffractograms result from Bragg's law being fulfilled and are evidence of a specific lattice spacing which can be characteristic for a mineral. The resulting diffractogram was corrected in the free graphical

interface software Profex which uses the BGMN Rietveld program (Döbelin and Kleeberg, 2015).

2.3 Scanning Electron Microscope (SEM) and Energy-Dispersive X-ray Spectroscopy (EDS)

SEM works by sending a focused high kinetic energy electron beam toward the sample area and detecting the outgoing electrons. The deceleration of these electrons produce many different signals; secondary electrons, backscattered electrons and characteristic X-rays. These signals can provide information on the morphology of particles from secondary or backscattered electrons (SEM), or the elemental composition from the X-rays (EDS) (Goldstein et al., 2017).

SEM and EDS were done at the Department of Geosciences, UiO. For SEM, a Hitachi SU5000 FE-SEM with a secondary electron detector was used and a voltage of 12 kV was applied, and for EDS a Dual Bruker Quantax XFlash 30 was used. High-resolution images with magnification in the range of 80x – 90 000x (corresponding to scales in images of 0.5 – 500 µm) were taken and EDS of points on selected particles were done of the carbon coated sample, which gives rise to a 0.277 keV peak. The pure Fh was observed with SEM at several areas of the sample to achieve a good description of the shape, size and degree of aggregation of the particles. The images were manipulated in a public domain image processing program ImageJ (Version 1.52a), where each visible particle in the image was counted and its apparent area measured relative to the scale set in the image. From the estimated 2D area of the particles, the particle diameter is assumed. This provided an

Figure 2: Processing of a SEM image of Fh in ImageJ. Top: Original image with a scale of 500 µm. Middle: The original greyscale image is set to binary. Bottom: The outlines of each individual particle is drawn.

approximation of the grain size distribution of the Fh particles. Only images with a representative overview of all particle sizes were used to estimate grain sizes. Figure 2 shows how the image processing was done in ImageJ. By making the original greyscale SEM images binary in color, the program utilizes contrast to determine the outlines of individual particles, and calculates the 2D area of the particles which was used to find particle diameter.
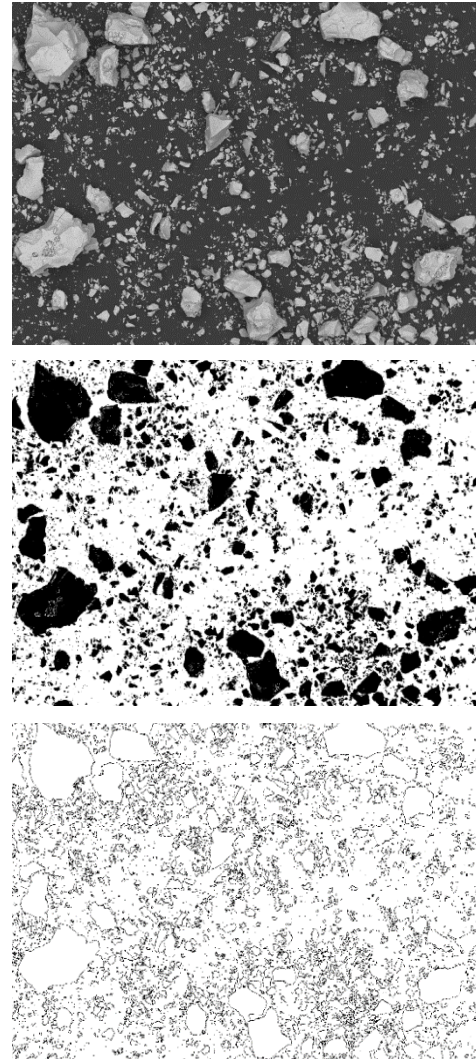
2.4 Attenuated Total Reflectance - Fourier-Transform Infrared (ATR-FTIR) Spectroscopy

FTIR is a technique for measuring the absorption in the infrared spectrum of a substance, collecting a large given range of the IR spectrum simultaneously. By directing IR radiation over a broad band at a substance, its molecular bonds will absorb some of the radiation by interacting with their dipole moment. The dipole moment changes when the molecule rotates and vibrates, and these rates of changing dipole moments have specific frequencies for a particular bond. The changing dipole moment interacts with the electric field of IR waves, and if the molecular bond frequency coincides with a frequency within the transmitted IR spectrum, this part of the transmitted band will be absorbed. Bonds can have several different frequencies as there are many rotational-vibrational modes. Stretching vibrations include symmetric and asymmetric stretching. Bending vibrations include scissoring, wagging, rocking and twisting. Attenuated Total Reflectance (ATR) – FTIR works by sending an IR beam through a crystal with a high refractive index causing reflections within the crystal, thus an evanescent field is generated which interacts with the sample until the beam exits the crystal. For ATR-FTIR to be possible, the crystal must have a higher refractive index than the sample material so there will be internal reflections. The evanescent field attenuates some of the light intensity of the IR radiation at certain frequencies determined by the sample. (Larkin, 2011b; Larkin, 2011a)

A Shimadzu IR Prestige-21 FTIR instrument with a Golden Gate single-reflection diamond crystal ATR module with a ZnSe lens was used at the Department of Chemistry, UiO. A small amount of the sample material was placed onto the diamond. Then the sample was clamped in place to ensure good contact with the diamond and to level the sample material. Between each experiment, the diamond and clamp were wiped clean with a damp paper towel and allowed to dry. Before each sample set was analyzed, a diamond/air background test was done to correct for the absorption bands produced by gas molecules in the atmosphere. Spectra were collected in the mid-IR region $4000 - 400$ cm^{-1}, and were run at 256 scans per sample with a resolution of 4 cm^{-1} to improve signal-to-noise ratio and to remove the variation in the background light. In addition to the spectra of the sorption experiments, the IR-spectra of the pure substances of Fh (solid) and PFCAs (all solid except for PFPeA which was in liquid state) were collected. In Shimadzu IR Solution v.1.50 the resulting interferograms were Fourier transformed, corrected for atmospheric noise and for the ATR method. The atmospheric correction mainly removes absorption by CO_2 and H_2O in the air. The ATR correction is an equation that takes into account the penetration depth of the evanescent wave into the sample, which requires the refractive index of both crystal and sample to be known, but an approximation of the samples' refractive index should provide decent results (Nunn and Nishikida, 2008).

The processing of spectra were done in R, a statistical computing program (R Core Team, 2020) with a spectroscopy package named ChemoSpec (Hanson, 2020). ChemoSpec is a General Public License free software package allowing simultaneous reading and processing of multiple spectra in R and was used for plotting and corrections of spectra.

2.5 Stock solutions of PFCAs and Fh

Perfluorinated pentanoic acid (PFPeA, $CF_3(CF_2)_3COOH$), perfluorinated octanoic acid (PFOA, $CF_3(CF_2)_6COOH$), perfluorinated nonanoic acid (PFNA, $CF_3(CF_2)_7COOH$) and perfluorinated decanoic acid (PFDA, $CF_3(CF_2)_8COOH$) analytical and reference standards were obtained from Sigma-Aldrich. A low-density polyethylene (LDPE) bottle was rinsed twice with milli-Q water. The PFCA stocks were made by weighing out 250 mg of the PFCA solids and dissolving it in 250 ml of milli-Q water, with the exception of PFPeA which was provided in liquid form by the manufacturer. The solutions were dissolved after a few hours of stirring using a magnetic stirrer, except for PFDA which required a couple of days of stirring to dissolve. A 2 g/l stock of PFPeA was made by pipetting 301 µl PFPeA and filling the 250 ml flask with milli-Q water until a volume of 250 ml was reached. PFPeA has a density of 1.713 g/ml and a purity of 97%. The mass of 301 µl of the pure PFPeA solution is then 0.301 ml * 1.713 g/ml * 0.97 ≈ 0.500 g, which dissolved in 250 ml of water, achieves a concentration of 2 g/l.

A suspension of 2 g/l of Fh was made by crushing the grains in an agate mortar, weighing out 500 mg of Fh and dispersing it in 250 ml of milli-Q water. The bottle was shaken vigorously before any amount was extracted to ensure the Fh particles were kept in suspension. Another, higher concentration, stock suspension of Fh was made the same way (2.5 g to 250 ml milli-Q water), at a 10 g/l concentration to test sorption when the amount of sorbent is in abundance.

For the sorption experiments, lower working concentrations were made. The PFCA stocks of 1 g/l were diluted at a ratio of 1:10 twice, to PFCA-B and PFCA-C at concentrations of 100 mg/l and 10 mg/l, respectively. This was done by pipetting out 1 ml of the PFCA-A, adding 9 ml of milli-Q water, and then taking 1 ml of the PFCA-B and adding 9 ml of milli-Q water to that. For the PFPeA stock, PFCA-A was made from the 2 g/l PFPeA solution by measuring out 125 ml and adding 125 ml of milli-Q water, achieving a 1:2 dilution. From there, the PFCA-B and -C for PFPeA were made as for the other PFCAs previously described.

Table 2: Stock solutions of perfluorinated carboxylic acids and ferrihydrite used for the sorption experiments.

Stock solution:	Concentration (mg/l)
PFCA-A	1000
PFCA-B	100
PFCA-C	10
Fh	2000

2.6 Sorption experiments for ATR-FTIR

2.6.1 Sorption onto Fh at various PFCA loadings

Three sets of experiments were done for sorption onto Fh at various PFCA loadings. The main set was done for all PFCAs with a Fh concentration at 1 g/l. The two other sets were only done for PFOA: one with Fh and PFOA concentrations exactly as the first set, but the sample material was dried before measuring with FTIR, and the other with increased Fh concentration at 5 g/l with the same PFOA concentrations as the other sets.

Six batch reaction experiments for PFCAs were carried out at concentrations of 1, 10, 100, 300, 500 and 1000 mg/l for the PFCAs and a constant concentration of 1 g/l of Fh. They were shaken for approximately four days. The stock and the working concentrations of PFCAs and Fh are shown in table 2. The specifics of concentrations and amounts of Fh and PFCA stocks added to achieve the desired final concentrations are given in table 3.

Table 3: Specific set-up for the sorption experiments onto Fh at varying PFCA loadings

Sample #	1	2	3	4	5	6
Fh suspension (ml)	5	5	5	5	5	5
PFCA stock (ml)	1 (PFCA-C)	1 (PFCA-B)	1 (PFCA-A)	3 (PFCA-A)	5 (PFCA-A)	-
Milli-Q (ml)	4	4	4	2	0	~5
Final [PFCA] (mg/l)	1	10	100	300	500	1000
Final [Fh] (mg/l)	1000	1000	1000	1000	1000	1000
Final volume (ml)	10	10	10	10	10	10

To achieve the highest concentrations (1000 mg/l, table 3), PFCA amounts of 10 mg were weighed directly and dissolved in 5 ml of water and 5 ml of Fh-suspension, except for PFPeA where the 2 g/l PFPeA solution was used directly. The high concentration solution of 2 g/l PFCA was difficult to attain by dissolving in water with a magnetic stirrer for the solid PFCAs which is why these were dissolved directly in the centrifuge tubes by vigorous shaking which seemingly was the more effective dissolution method.

For the first set of sorption experiments, 5 ml of 2 g/l Fh suspension was added to all centrifuge tubes to achieve 1 g/l in the final volume of 10 ml. The 500 mg/l PFCA sorption samples were made by adding 5 ml of 1000 mg/l PFCA-stock (PFCA-A) to the Fh suspension. The 300 mg/l samples were made by adding 3 ml of 1000 mg/l PFCA-stock (PFCA-A) to the Fh suspension and filling with 2 ml of milli-Q water. The 100 mg/l samples were made by adding 1 ml of 1000 mg/l PFCA-stock (PFCA-A) to the Fh suspension and filling with 4 ml of milli-Q water. The 10 mg/l samples were made by adding 1 ml of the 100 mg/l PFCA-stock (PFCA-B) to the Fh suspension and filling with 4 ml of milli-Q water. The 1 mg/l samples were made by adding 1 ml of 10 mg/l PFCA-stock (PFCA-C) to the Fh suspension and filling with 4 ml of milli-Q water. After shaking for an appropriate amount of time, supernatant fluid was pipetted off until a spreadable Fh/PFCA slurry was left.

The second set of sorption experiments followed these exact concentrations except that these were dried in an oven at 40 °C before measuring with FTIR. The third set of sorption experiments were done with a 5 g/l Fh suspension, but otherwise the same PFOA concentrations and PFOA/water/Fh solution volumes were used.

2.6.2 ATR-FTIR of pure PFCAs and ferrihydrite

IR spectra of the pure PFCAs and of Fh were collected. All PFCAs except PFPeA are solids in their pure form, and were directly placed onto the diamond crystal and clamped down, as was the pure Fh. A small amount of the pure liquid PFPeA was pipetted onto the crystal and the clamp was not fastened all the way to ensure there was still sample material on the diamond.

2.6.3 From ATR-FTIR to sorption isotherms

ATR-FTIR experiments were done at varying PFCA loadings to observe the relationship between aqueous concentration vs. sorbed amount, and from them produce sorption isotherms. While absorbance cannot directly measure concentrations of substances, there is some basis for quantitative analyses – the Lambert-Beer law. The Lambert-Beer law (Eq. 1) relates the light attenuation of a material, in this case absorbance, A, to its molar attenuation coefficient, ε, optical path length, ℓ, and molar concentration of sample material, c. The molar attenuation coefficient is a constant inherent property of a material dependent on wavelength of the transmitted light. The optical path length is dependent on the refractive indices of the materials it propagates within and will ideally not vary too much between samples of similar content. Molar concentration is therefore the variable that should change the resulting absorbance most due to the varying PFCA loadings. (Larkin, 2011b)

$$A = \varepsilon \ell c \qquad\qquad Eq.\ 1$$

When the relationship between molar concentration and absorbance has been established, taking the varying initial dissolved concentrations of PFCA and plotting them as a function of absorbance of the solid sorbed sample should provide an approximation of the sorption isotherms. The area under the CF-related absorption peaks will be used as the total absorbance of PFCAs onto ferrihydrite for the sample.

The area between $1270 - 1110$ cm^{-1} was chosen as the most reliable zone for capturing the total absorbance for all PFCAs as this was the zone with most intense CF absorbance and where the first appearances of peaks occurred. In addition, there is little other absorption of significance there that could cloud the results. The spectra were baseline-corrected so the relative absorption could be found. Then, a sum of a series of Gaussian functions (Eq. 2 and figure 3) were fitted to the spectra, where a_i is the absorbance, b_i is the mean band position and c_i is the standard deviation for peak i. Each function corresponds to an absorption peak in the spectra (figure 3a) and the sum of them (figure 3b) is a mathematical approximation of the spectra. The number of functions, n, for a given spectrum depends on how many peaks were
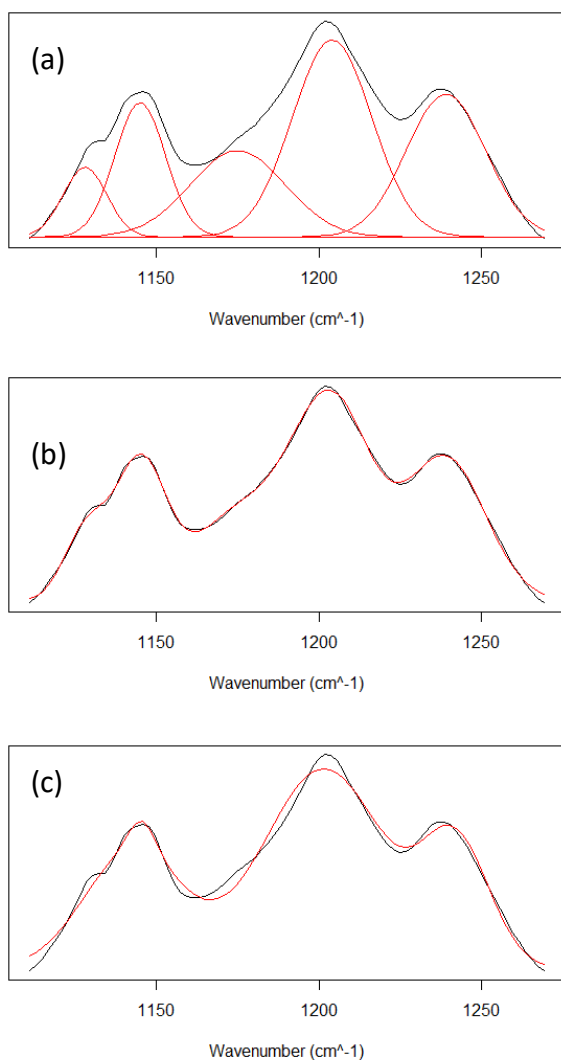
Figure 3: Black lines are the recorded absorption spectrum of PFOA and red lines are the Gaussian function fits. (a) The Gaussian functions plotted separately. (b) Sum of all Gaussian functions. (c) Sum of Gaussian functions without accounting for the break/underlying absorption peak around 1175 cm^{-1}.

visible in the region. The number of functions/peaks varied between 2 – 6, depending on concentration and to achieve the best approximations.

$$\sum_{i=1}^{n} a_i e^{-\frac{(x-b_i)^2}{2c_i^2}} \qquad Eq.\ 2$$

There were several occasions where the smaller peaks were not fully located, and not discovered until the Gaussian functions were fitted. An example of this is in the absorption spectrum of PFOA where a sum of 4 functions was fitted initially (figure 3c) and was off at a number of points, but when a fifth function was added around 1175 cm^{-1}, this was corrected (figure 3b). Figure 3a shows the individual contributions of the peaks to the total absorption. The total absorbance in the CF-region for a given sample was normalized to the number of CF-moieties for the molecule, i.e. 4, 7, 8 and 9 for PFPeA, PFOA, PFNA and PFDA, respectively. Absorbance in the CF-region is dependent on all contributions from CF$_3$+(CF$_2$)$_n$, and absorbance can only provide a rough approximation of concentration.

$$C_s = K_f C_w^n \qquad Eq.\ 3$$

The resulting areas of absorbance were plotted against initial PFCA concentrations, and from there an exponential function was fitted to the data to obtain the Freundlich sorption isotherms (Eq. 3), where C_s is the sorbed PFCA concentration (mg/kg), K_f is the Freundlich distribution coefficient (L/kg), C_w is the aqueous PFCA concentration (mg/l) and n is a constant describing the non-linearity of sorption. From the Freundlich isotherms the equilibrium constants for the sorption of PFCA to Fh can be found which can be used in geochemical modeling.

2.7 Solid Phase Extraction Liquid Chromatography Tandem Mass Spectrometry (SPE-LC-MS/MS) – Sorption of PFOA and PFDA to Fh

SPE-LC-MS/MS is a method with low LOD for determining concentrations in liquid samples. The solid phase extraction allows sorbed material to be extracted from solid to liquid phase using a solvent (extraction liquid) and subsequently to be measured by LC-MS. The sorption samples were prepared at the department of geology, UiO, but LC-MS and specific method preparations were conducted externally at the Norwegian University of Life Sciences

(NMBU). The samples were analyzed with an Agilent 6460 Triple Quadrupole and an attached Agilent 1200 HPLC. Two mobile phases were used: 10% methanol + 2 mM ammoniumacetate (A) and ~100% methanol + 2 mM ammoniumacetate (B). Mobile phase A is used during sample measurement at a constant flow rate and phase B is used to flush the column (Shoemaker and Tettenhorst, 2020).

The sorption samples were prepared exactly as for FTIR, but only for PFOA and PFDA at 1, 10, 100 and 500 mg/l, and only solid phases of 1 mg/l and 10 mg/l PFCA were measured. The reaction time, shaking, centrifuging etc. was the same as for FTIR. After centrifuging, the water samples were passed through 0.45 µm filters.

Sample mixtures were made of all water samples with the same PFCA concentration at a total of four samples for 1, 10, 100 and 500 mg/l PFCA at NMBU before measuring. These were further diluted with methanol to a total dilution factor of 6, 30, 300 and 1500 for the 1, 10, 100, 500 mg/l PFCA, samples, respectively. After dilution and right before sample measuring, stable isotope internal standards were added, samples were filtered with Spin-X centrifuge tubes and finally analyzed with LC-MS.

The solid Fh samples with sorbed PFCAs were centrifuged and supernatant water was removed with a pipette, and were allowed to dry for a day under a fume hood. From here, stable isotope internal standards were added right before the extraction process. The samples were extracted twice with methanol using a vortex mixer and 15 min in an ultrasound bath followed by centrifugation and filtration, and were analyzed with LC-MS.

Linear models were fitted for the resulting aqueous concentrations and solid amounts of PFCAs to yield equilibrium constants for PFOA and PFDA to Fh.

2.8 Density-functional theory (DFT) calculation of PFOA

Three DFT analyses were carried out of PFOA with Gaussian 09 (Frisch et al., 2010) by the senior engineer for environmental sciences at the Department of Chemistry, UiO. One analysis each for PFOAs protonated acid monomer, dimer and deprotonated anion. From the analyses, theoretical vibrational frequencies and spectra of PFOA in a vacuum were found. The combination of hybrid functional and basis set used for the calculation calls for a vibrational frequency scaling factor of 0.955. DFT results of PFOA were used complementary to the literature for interpretations and uncertainties of band assignments.

2.9 Modeling sorption of PFCAs onto Fh in PHREEQC

PHREEQC v3 (Parkhurst and Appelo, 2013) is a computer program created by the United States Geological Survey (USGS) that can model a variety of geochemical situations using batch-reactions, speciation and transport simulations through a chemically defined volume. It can be an excellent tool for predicting distribution of chemical species in the environment if the system is well defined. There are many thermodynamic libraries for different compounds in PHREEQC-databases. These can be combined and modified to achieve the best approximation of an environmental situation.

The sorption isotherms provide parameters K_f and n from Eq. 3 and describes adsorbate-adsorbent mass ratios for a given concentration in a PFCA/Fh-system at equilibrium. The parameters were added to the PHREEQC.dat database (appendix, Section B) in order to simulate environmental transport situations.

The chosen environmental situation for the simulation was a fire-fighting practice facility by the Gardermoen airport. The ground and groundwater at this site is severely polluted both by jet fuel (Kłonowski et al., 2008) and aqueous film-forming foams (AFFF) (Norwegian Pollution Control Authority, 2008) which contains PFAS. As a result there have been several surveys in the area to characterize the hydrogeological conditions. This model will not try to simulate AFFF contamination where many PFAS exist at various amounts, but rather evaluate sorption of the PFCAs of different chain length at the same weight concentrations. The model will try to predict the amount of pore volumes and the how much time it takes for the contaminants to reach the end of a defined aquifer. The nearest recipient from the fire-fighting facility is the Sogna river approximately 1 km away from the contaminated site. Properties of the Gardermoen unconfined aquifer used in the transport simulation can be seen in table 4.

Table 4: Hydrogeological properties of the Gardermoen aquifer situated by the firefighting practice facility. Hydraulic conductivity, hydraulic gradient and groundwater velocity has been estimated by Kłonowski et al. (2008), bulk density and porosity of the soil by Knudsen (2003) and iron oxyhydroxide content by Søvik and Aagaard (2003).

Hydrogeological properties of the Gardermoen aquifer	
Hydraulic conductivity, K	Min. $1.17*10-4$ m s^{-1}
	Max. $1.37*10-2$ m s^{-1}
Hydraulic gradient, dh/dl	Min. 0.004384 m m^{-1}
	Max. 0.005208 m m^{-1}
Bulk density of soil, ρ_b	1.68 g/cm^3
Soil porosity, n	0.367
Mean groundwater velocity, v	10^{-5} m/s
Fe-oxide (%)	Min. 0.02
	Max. 1.0

PHREEQC defines a SOLUTION block with concentrations to a liter of water, so the amount of ferrihydrite added needs to be as well. The amount of sediment per liter of water, assuming saturated conditions, is (1-0.367)/0.367 = 1.725 L sed/L water. The average iron oxide content of the Gardermoen soil is close to 0.2 % Fe (Søvik and Aagaard, 2003) and all iron oxides will be considered as 2-line Fh. The amount of Fh in contact with 1 liter of water is 1.725 L sed * 1680 g/dm^3 * 0.002 = 5.8 g. Molar mass of 2-line Fh is disputed as it can vary with water content, but 101 g/mol Fe is a reasonable approximation (Hiemstra and Van Riemsdijk, 2009). The amount of binding sites per mole of Fe is around 0.2 according to Dzombak and Morel (1990). The estimated amount of Fh in contact with 1 L of groundwater is hence 5.8 g $\div$ 101 g/mol * 0.2 $\approx$ 0.0115 mol, which is the amount of Fh equilibrated to each cell in the aquifer.

The TRANSPORT block in PHREEQC allows modeling of 1D-transport including advection, dispersion, diffusion and reactions. It is described as an upwind-scheme where a column is defined by a number of cells and per shift, each solution is moved to the next cell until SOLUTION 0 has been moved to cell 1 (Parkhurst and Appelo, 2013). For the sake of simplifying the model, only advective transport in the saturated zone has been considered and diffusion and dispersion parameters are set to 0. The model only considers equilibrium soil-water transport, i.e. pure compounds and vapor phase are not accounted for. An initial SOLUTION 0 is defined with PFCA contaminant concentrations set to the highest experimental concentrations of 1000 mg/l. The aquifer is defined as SOLUTION 1-10 with an initial composition of pure water and is equilibrated with SURFACE 1-10 which contains the Fh. The TRANSPORT block has 10 cells corresponding to SOLUTION 1-10, and the cell length is 1 m. With 10 cells at 1 m length, the total length of the aquifer is thus 10 m. SOLUTION 0 is then transported through the defined column and equilibrated with SURFACE/SOLUTION 1-10 throughout all cells and equilibrated at each step. SOLUTION 0 is continually shifted into the aquifer and represents a point source of contamination that does not deplete. Different results can be extracted from PHREEQC, i.e. time, shifts, distance, amounts/concentrations of species in any solution/surface. The transport simulation results were plotted from the last cell with sorbed amounts and concentrations of PFCAs vs. number of pore volumes and time.

Input file with comments:

```
SOLUTION 0                #Contaminated water
     units mol/l
     pH    7      charge
     Pfpea 3.787e-3   # 1000 mg/L
     Pfoa  2.415e-3   # 1000 mg/L
     Pfna  2.154e-3   # 1000 mg/L
     Pfda  1.945e-3   # 1000 mg/L

SOLUTION 1-10
     pH    7      charge

SURFACE 1-10 # Ferrihydrite surface
     -equilibrate 1
     Z     0.0115    450   5.8   # Fh 0.2 sites/mole Fe
                                 # Dzombak and Morel (1990),
                                 # SSA: 450 m2/g,
                                 # 5.8 g Fh normalized to 1 L of GW in
                                 # soil with iron oxide content of 0.2%
                                 # from Søvik and Aagaard (2003),
                                 # soil porosity 0.367 and
                                 # d = 1.68 g/cm3. Porosity/density from
                                 # Kłonowski et al. (2008).
                                 # Mm(Fh) = 101 g/mol Fe from
                                 # Hiemstra and Van Riemsdijk (2009)
END

TRANSPORT 1
     -cells 10               # Number of cells
     -shifts 100            # Number of times solutions are "shifted"
                            # through reservoar cells.
     -time_step 100000      # Time per shift, here 27,77 hours or a GW-
```

```
                                    # velocity of 1 m / 10e5 s = 10e-5 m/s
        -lengths      1             # Length of cell (m)
        -dispersivities    0
        -diffusion_coefficient 0
        -punch_cells 10             # Only punch results from last cell, i.e. 10 m
                                    # from point source
        -punch_frequency 1         # Punch results every shift
END
```

3. Results

3.1 X-Ray Powder Diffraction

The diffractogram for 2-line ferrihydrite is shown in figure 4. There are broad peaks at Bragg angles 35° and 62°, corresponding to lattice spacings of 2.56 Å and 1.49 Å, respectively, which is characteristic of 2-line ferrihydrite (Villacís-García et al., 2015; Manceau and Drits, 1993; Vaughan et al., 2012). There is an increase in intensity toward lower angles and then a sudden sharp decrease from 13° - 0°.
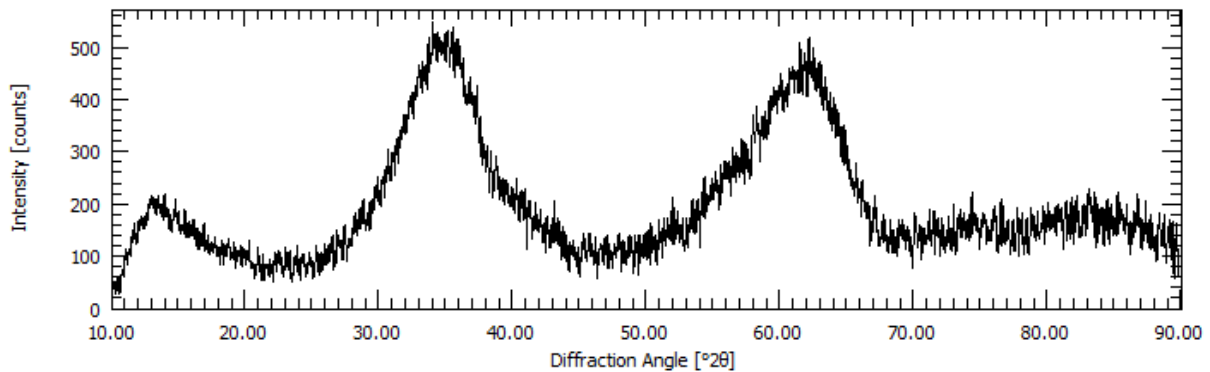

Figure 4: X-ray Powder Diffraction. Diffractogram of 2-line ferrihydrite with broad peaks at Bragg angles 35° and 62°.

3.2 Scanning Electron Microscopy

The images show varying grain sizes and some aggregation of ferrihydrite (figure 5). There are many nanoparticles, but also some particles larger than 100 μm. Some of the larger particles are composed of a single large grain and others are aggregates of smaller particles. From the counts made by ImageJ, the estimated amount of grains of nanoparticle size (< 1μm) was more than 89%. The particles have sharp edges and the surfaces of the aggregates appear very rough.
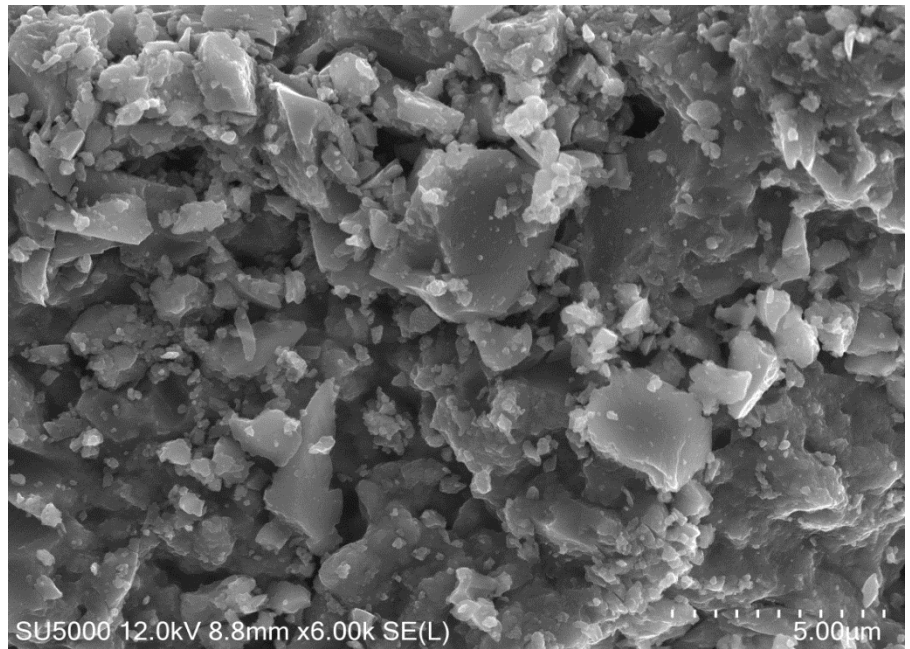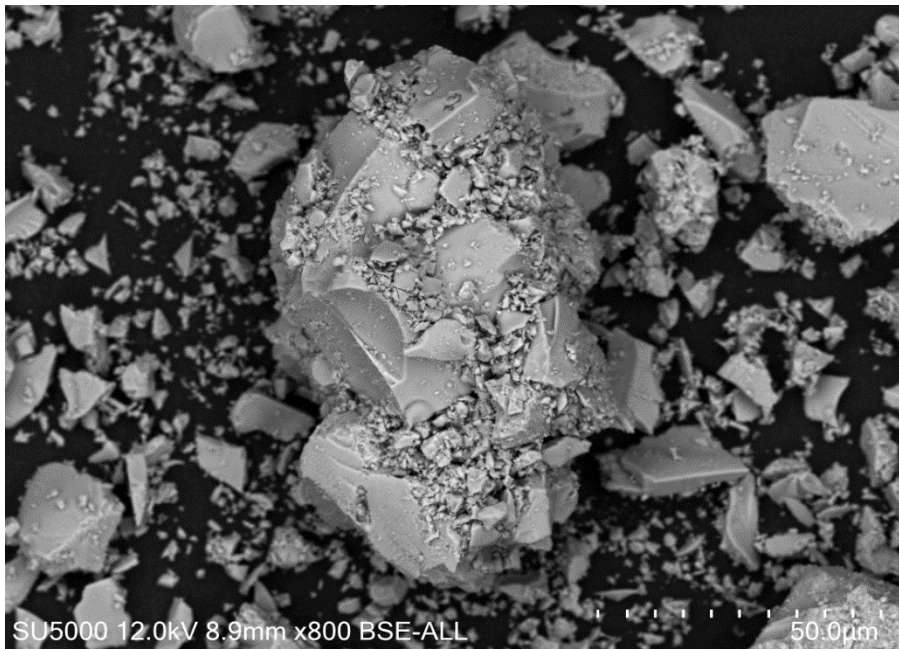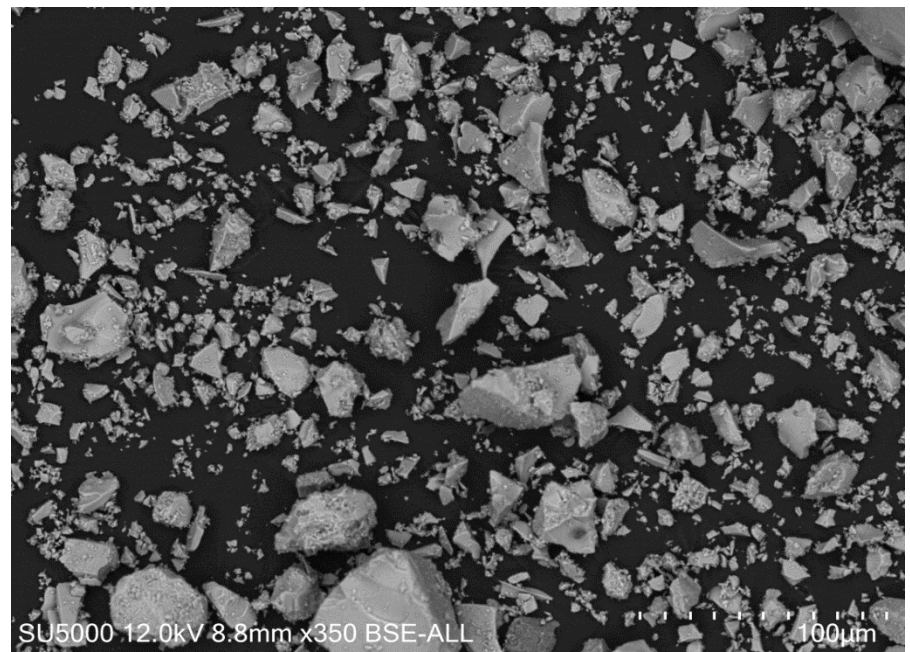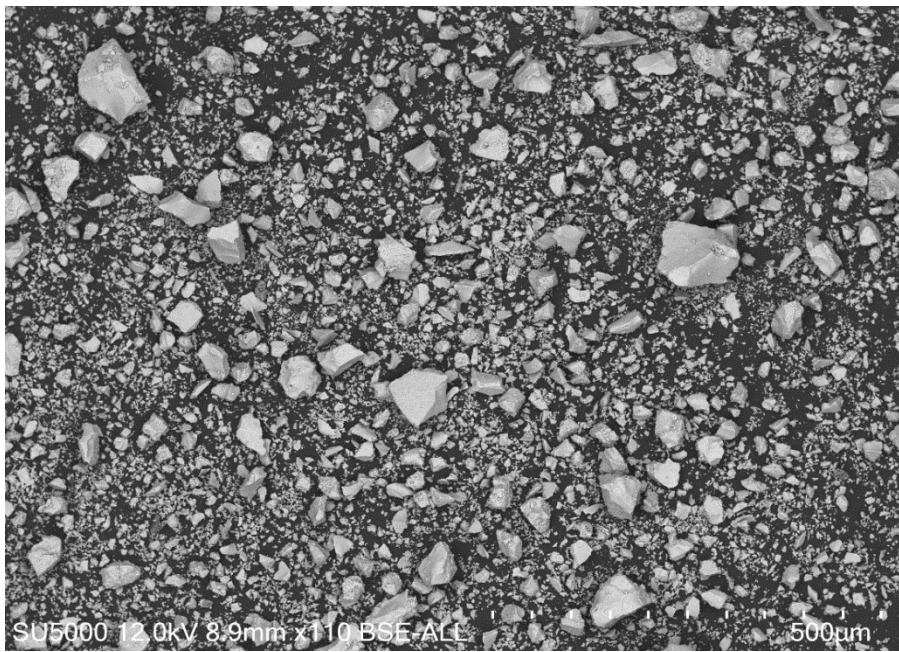
Figure 5: SEM images of ferrihydrite at various magnifications. A scale is displayed in each image in the lower right corner and magnification and detection mode in the lower left.
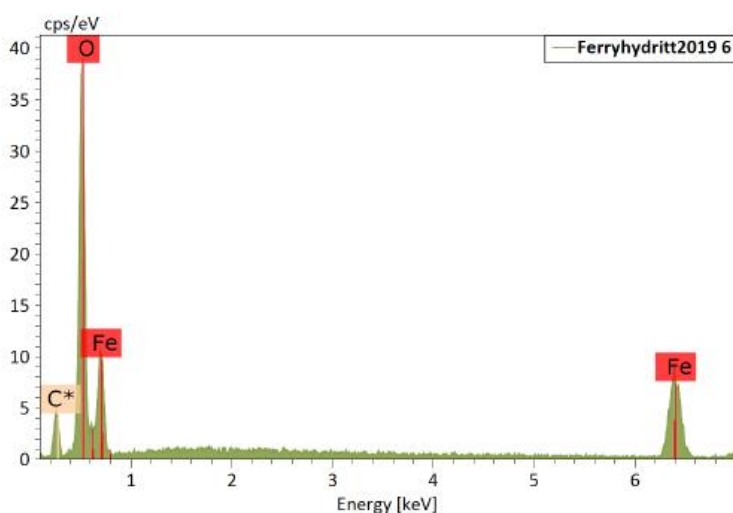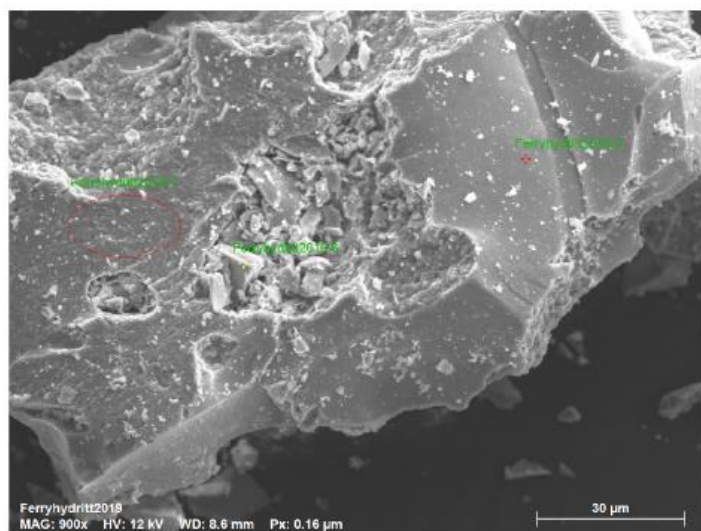
3.3 Energy-Dispersive X-ray Spectroscopy

EDS of a ferrihydrite grain is shown in figure 6. The oxygen peak at 0.5 keV is due to O K_α and the two iron peaks at 0.7 keV and 6.4 keV are due to Fe L_α and K_α, respectively. EDS-analyses of a 3D sample particle are semiquantitative and only provide an indication of the relative amounts of elements present. Hydrogen atoms, which are likely present in the Fh particles as part of structural water, do not emit X-rays (Goldstein et al., 2017).

3.4 Attenuated Total Reflectance – Fourier Transform Infrared Spectroscopy

Spectra of the sorption samples as well as the pure, unreacted Fh and PFCAs were collected. The sorption samples will be assigned absorption frequencies separately, but will share most of the same properties.

3.4.1 IR spectra of Fh and the PFCAs

Notation, wavenumbers and sources for the mode assignments can be viewed in table 5. The entire spectra of the pure, isolated substances have been compiled in figure 7. The three main IR ranges of interest are the region at 4000 – 2500 cm^{-1} for water, hydroxyl and hydrogen bonding frequencies, and the region for the carboxylate functional group which absorbs light between 1800 – 1300 cm^{-1}, and lastly the fingerprint region of PFAS which lies between frequencies of 1400 – 1000 cm^{-1} (Socrates, 2001; Larkin, 2011d). Some additional spectra can be found in figure 16 and figure A 1-4.
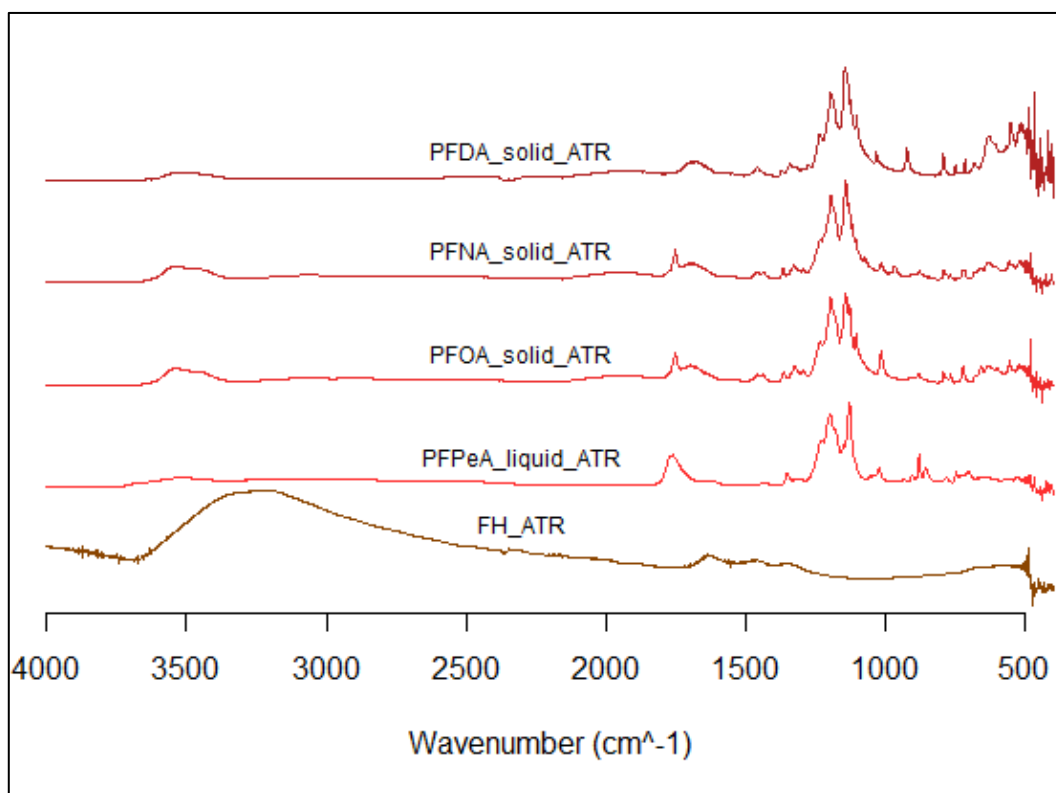
Figure 7: ATR-FTIR absorption spectra of solid Fh and PFCAs (except for liquid PFPeA). IR region: 4000 - 500 cm^{-1}. Spectra are plotted with an offset and amplitudal gain.

Water has a very broad band covering the range from ~4000 - 3000 cm^{-1} due to stretching vibrations and hydrogen bonding, and another band, although not as broad and intense, around 1645 cm^{-1} due to H-O-H bending vibration (Max and Chapados, 2009). Ferrihydrite, as the name implies, incorporates water in its mineral structure which contributes to the observed peaks at ~3250 cm^{-1}, but is mostly due to adsorbed water together with $v_b(H_2O)$ at 1634 cm^{-1}. The peaks at approximately 3540 cm^{-1} and 3440 cm^{-1} for the PFCAs are due to OH-stretch (Larkin, 2011d), and the broadness of the peaks indicate hydrogen bonding (Coates, 2006; Kollman and Allen, 1972). The pure PFCAs show little influence of water-assigned bands, but do exhibit a low intensity (not very visible as a result) broad band over 3300 – 2450 cm^{-1} which is associated with OH-bending in hydrogen-bonded carboxylic acid dimers (Larkin, 2011c; Shipman et al., 2007), but this will be delved into later in the discussion.
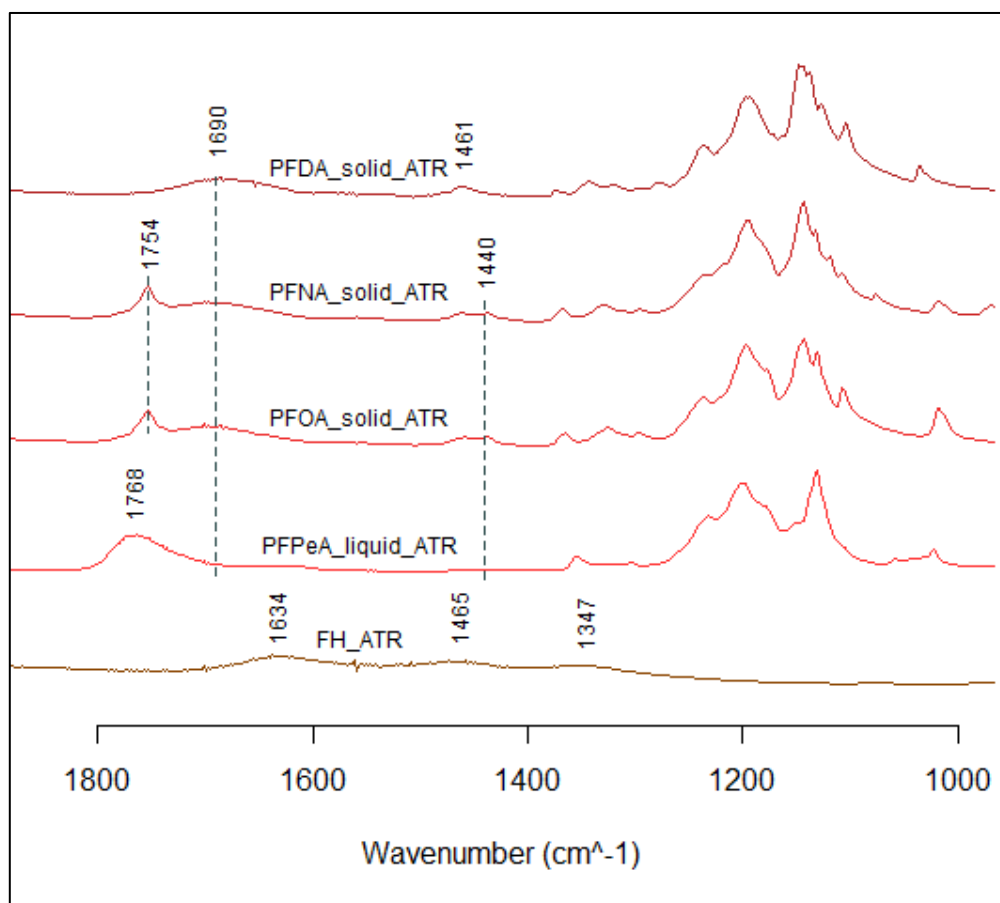
20

Figure 8: ATR-FTIR absorption spectra of the pure PFCAs and ferrihydrite. IR region: 1800 – 1000 cm^{-1} .

The spectra in the region of 1800-1000 cm^{-1} for the pure substances are shown in figure 8. A carboxylic acid group contains a C=O and an O-H bond and, in the case of PFCAs, bound to a perfluorinated carbon chain. C=O stretch vibration for the PFCA monomers falls between approximately 1755-1768 cm^{-1}, while it appears redshifted for dimers (Larkin, 2011c). Monomers are also characterized by having stronger absorbance than hydrogen-bonded dimers (Shipman et al., 2007). PFPeA shows greater absorption intensity toward the monomeric state, whereas PFNA and PFOA show some monomeric behavior as well as dimer absorption. PFDA shows no absorption from monomers and only exhibits absorption that is expected from a dimeric structure. The peak at 1440 cm^{-1} is likely due to C-O-H–bending in carboxylic acids and peaks at ~1460 cm^{-1} could be due to CH_2-bending (Larkin, 2011c) from incomplete fluorination.

The absorption peaks for ferrihydrite at 1634 cm^{-1} is due to $v_b(H_2O)$, and 1465 cm^{-1} and 1347 cm^{-1} are due to sorbed inorganic carbonates' symmetric and asymmetric C-O stretch vibrations, respectively (Villacís-García et al., 2015; Socrates, 2001).

Table 5: Assignment of modes to absorption peaks for the spectra of pure PFCAs. Stretch vibration (v), asymmetric (as), symmetric (s), bend (b).

Mode of rotation or vibration	Wavenumber (cm^{-1})	Relative intensity, shape
v(OH) monomeric	~3450 and ~3540	Medium, broad
v_s(H$_2$O)	~3250	Weak/medium, very broad
v(C=O) monomeric carboxylic acid	1754 – 1768	Strong, narrow
v(C=O) dimeric carboxylic acid	1685 – 1695	Strong/medium, broad
v_b(H$_2$O)	~1634	Weak (but dependent on water content), broad
v_s(C-O) carbonates	1465	Weak/medium, broad
v_{as}(C-O) carbonates	1347	Weak/medium, broad
v_{as}(CF$_2$)	1235 – 1238	Strong, narrow
v_{as}(CF$_2$+CF$_3$)	1198 – 1202	Strong, narrow
v_s(CF$_2$)	1145 – 1148	Strong, narrow
v_{as}(CF)	1178 and 1131	Weak and medium, narrow
v(CF$_3$)	1119	Medium, narrow

Assignment sources: water and OH (Max and Chapados, 2009; Socrates, 2001), carboxylic acids (Cabaniss and McVey, 1995; Max and Chapados, 2004) and C-F (Gao and Chorover, 2012; Danilczuk et al., 2011; Beg and Clark, 1962), carbonates (Villacís-García et al., 2015).

Spectra in the region of 1300-1100 cm^{-1} for the isolated PFCAs are shown in figure 9. The most important assignments of absorption peaks from ATR-FTIR for the interpretation of sorption and binding mechanisms of PFCAs are given in table 6. Additional spectra with interpretations and uncertainties will be discussed. The three most prominent PFCA-related peaks appear at wavenumbers of approximately ~1146 cm^{-1} (not present for PFPeA), ~1198 cm^{-1} and ~1238 cm^{-1}, representing symmetric CF$_2$-stretching, the combined asymmetric CF$_2$+CF$_3$-stretching and asymmetric CF$_2$-stretching vibrations, respectively (Gao and Chorover, 2012; Danilczuk et al., 2011; Beg and Clark, 1962). The PFCAs show narrower as well as more intense peaks as the concentrations increase.

PFPeA, PFOA, PFNA and PFDA all show similar absorption patterns, but PFPeA differs in some respects. The peak at ~1146 cm^{-1} for PFDA is seemingly split into two components at 1144 cm^{-1} and 1148 cm^{-1}, which is not as recognizable in the spectra of the other PFCAs, and will for now only be assigned to symmetric CF$_2$ stretch vibration. The most striking difference between the IR spectrum of PFPeA and the other PFCAs is the lack of the peak at 1146 cm^{-1} in favor of a very prominent peak at 1131 cm^{-1}, which is assigned to asymmetric CF-stretch vibration. PFPeA does have a small bump around ~1150 cm^{-1}. The peak position at 1201 cm^{-1} for PFPeA has a slightly higher band position than the corresponding peak for the other PFCAs. (Gao and Chorover, 2012; Danilczuk et al., 2011; Beg and Clark, 1962).
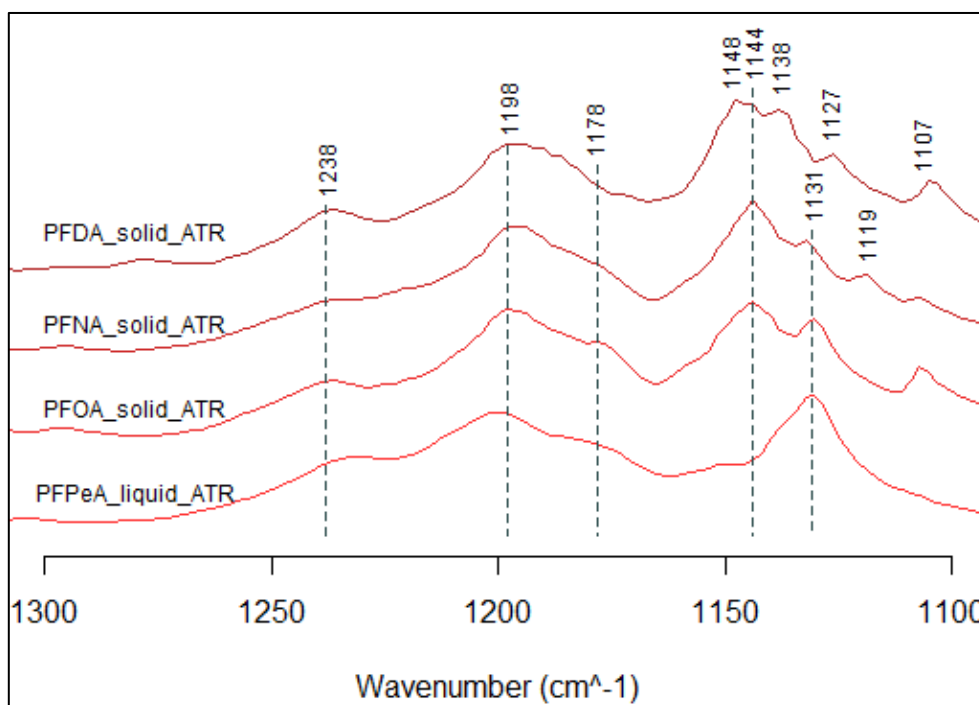
Figure 9: ATR-FTIR absorption spectra of the pure PFCAs. IR region: 1300 - 1100 cm⁻¹. The spectra are plotted with an offset for better visualization and the absorbance intensities are only qualitative.

3.4.2 IR spectra for sorption experiments at varying PFCA loadings

The full spectra from the sorption experiments show clear evidence of water content, by having a very broad absorption band over ~3200 cm⁻¹ and ~1634 cm⁻¹ due to $v_s(H_2O)$ and $v_b(H_2O)$, respectively. The sorption experiments for PFOA have higher relative intensity of water bands due to wetter samples. The full assignment of CF-related peaks are similar to that of the pure substances, and will not be reiterated, but can be found in figure 10 and table 6.

PFOA, PFNA and PFDA show similar absorption patterns, but PFOA slightly differs. Whereas PFNA and PFDA have broader and somewhat merged peaks at ~1205 cm⁻¹ and ~1238 cm⁻¹, PFOA shows two distinct peaks. Furthermore, the peak at 1145 cm⁻¹ for PFOA is (as with PFDA for the pure substances) split into two components. The spectra for PFDA at the highest initial concentration of 1000 mg/l shows highly increased absorption intensities across the whole PFCA-related spectrum.

The most prominent peaks for the sorption experiments with PFPeA are at wavenumbers ~1134 cm⁻¹, 1201+1214 cm⁻¹ and 1238 cm⁻¹. The absorption peak at ~1160 cm⁻¹ can either be due to asymmetric or symmetric CF₃-stretching (Beg and Clark, 1962). For all other PFCAs, the symmetric CF₂-stretch is around 1146 cm⁻¹ (Gao and Chorover, 2012). The absorption peak at 1118 cm⁻¹ only occurs for PFNA.

There is a red shift of the peaks for the highest concentrations of PFNA and PFDA which is why these vertical lines do not perfectly intersect the peaks for the highest concentrations, and why there is an independent label for the band position of the severely shifted peak.
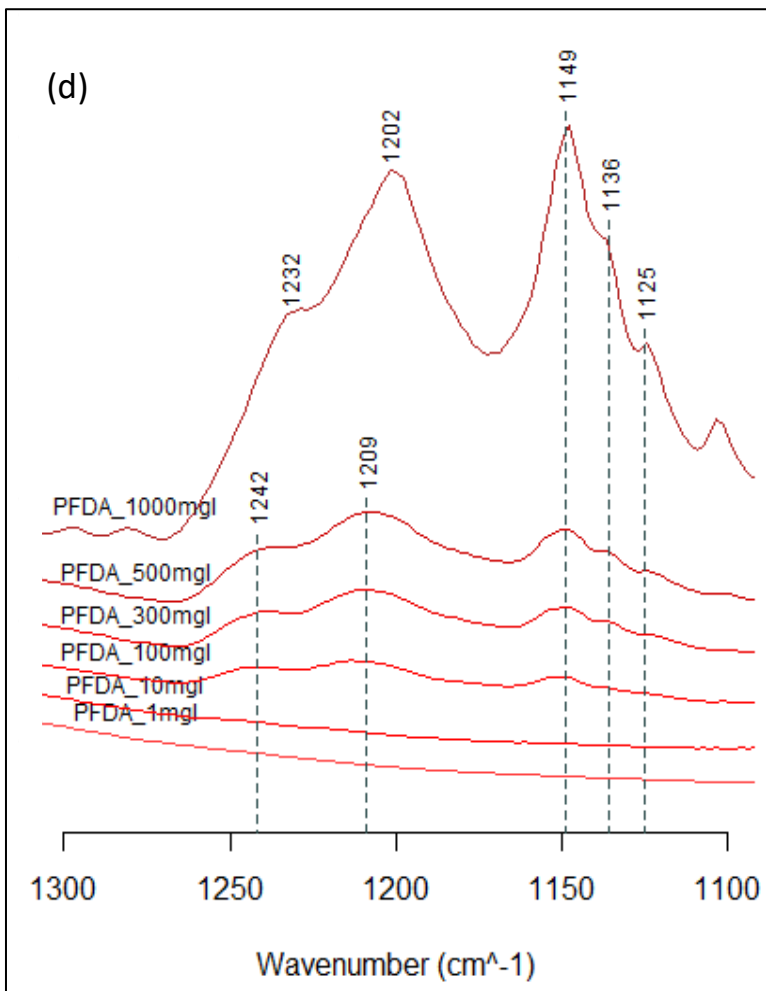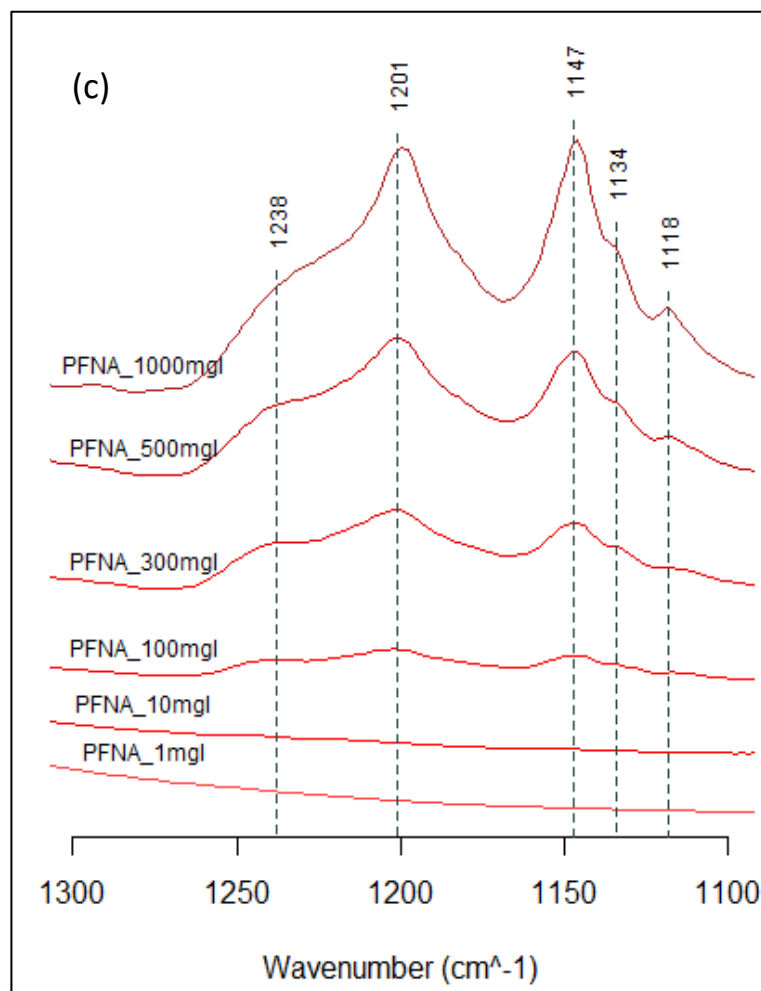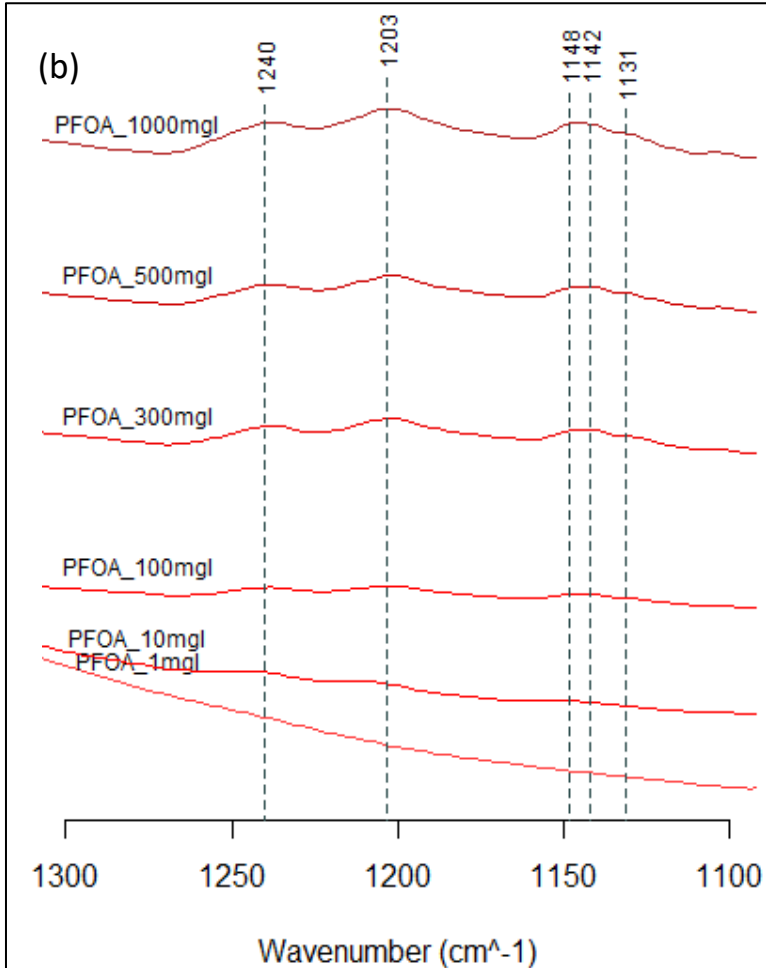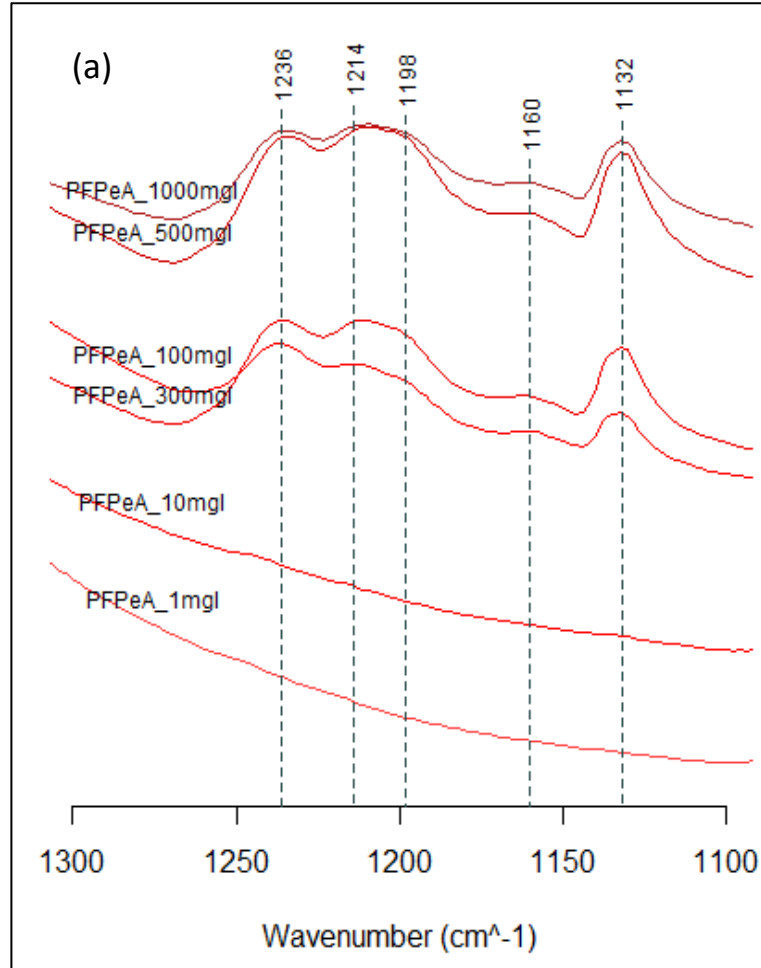
Figure 10: (a) PFPeA (b) PFOA (c) PFNA (d) PFDA. ATR-FTIR absorption spectra of PFCAs from the sorption experiments at varying loadings. IR region: 1300 - 1100 cm^{-1}. The spectra are plotted with an offset between eachother for clear visualization, so exact values for absorbance are removed.

Table 6: Assignment of modes to absorption peaks for the spectra of the sorption experiments. Stretch vibration (v), asymmetric (as), symmetric (s), bend (b).

Mode of rotation or vibration	Wavenumber (cm^{-1})	Relative intensity, shape
$v_s(H_2O)$	~3200	Strong, broad
$v_b(H_2O)$	~1634	Medium, broad
$v_{as}(COO^-)$	1650	Strong to medium, broad (but narrow for some high concentrations)
$v_s(C-O)$ carbonates	1465	Weak to medium, broad
$v_s(COO^-)$	1344 - 1368	Weak to medium
$v_{as}(C-O)$ carbonates	1350	Weak to medium, broad
$v_{as}(CF_2)$	1236 - 1242	Strong
$v_{as}(CF_2+CF_3)$	1201 - 1209	Strong
$v_s(CF_2)$	1142 - 1149	Strong
$v_{as}(CF)$	1175 and 1131	Weak to medium
$v(CF_3)$	1118	Medium

Assignment sources: water (Max and Chapados, 2009), carboxylic acids (Cabaniss and McVey, 1995; Max and Chapados, 2004) and C-F (Gao and Chorover, 2012; Danilczuk et al., 2011; Beg and Clark, 1962), carbonates (Villacís-García et al., 2015).

The covalent bonds between carbon and the two oxygens in a carboxylate group have bond number 1.5 because a third electron pair is shared between them, and each CO bond is therefore a "bond and a half". The COO$^-$ frequencies of interest occur at 1634-1650 cm^{-1} and 1344-1368 cm^{-1} (figure 11) corresponding to the asymmetric and symmetric "bond and a half" stretch vibrations of CO, respectively, and are reported as $v_{as}(COO^-)$ and $v_s(COO^-)$ (Max and Chapados, 2004; Gao and Chorover, 2012). They co-occur as a doublet for deprotonated carboxylic acids, and the difference in band position between the asymmetric and symmetric COO$^-$ stretch is termed Δ, $v_{as}(COO^-)$ - $v_s(COO^-)$. The Δ is around 305 cm^{-1} for PFPeA and 281 cm^{-1} for PFNA and PFDA. The $v_{as}(COO^-)$ peak for PFOA is masked by the peak for water bending deformation because these samples were wetter than the others when measured, but it is highly likely that the $v_{as}(COO^-)$ absorption peak occurs somewhere between 1635 – 1650 cm^{-1}. The grey lines in figure 11 mark the first appearance of a band shift which usually occurred after PFCA concentrations of 100 mg/l and higher. The $v_s(COO^-)$ is visible for all PFCAs around 1344 - 1368 cm^{-1}, but is not visible for any of the PFCAs at the two lowest PFCA loadings and its band position does not change after appearing. PFDA shows a sudden change in shape of absorption peaks for the highest concentration, as can be seen both for the CF- and carboxylate-region.
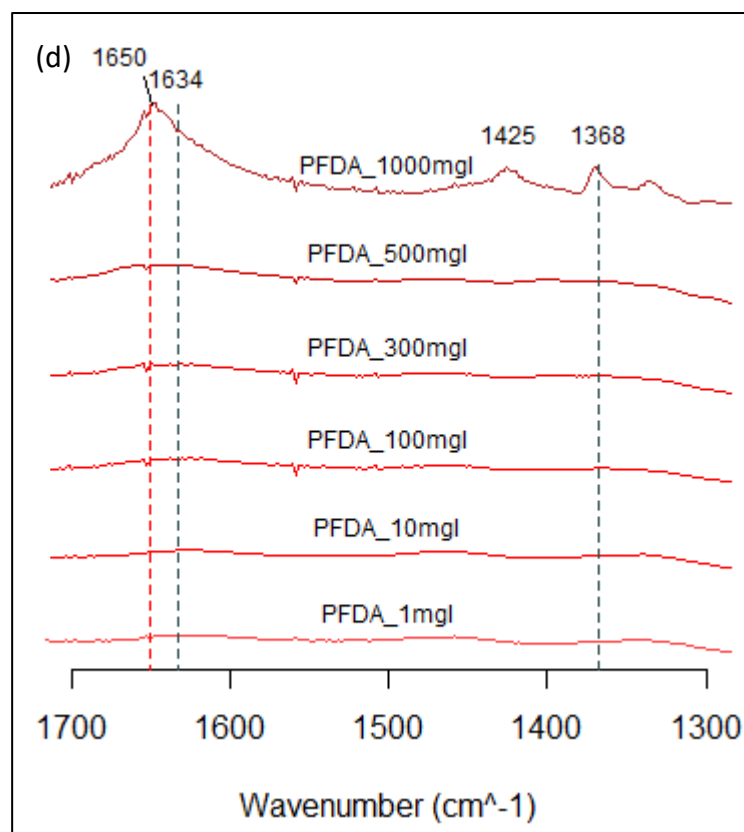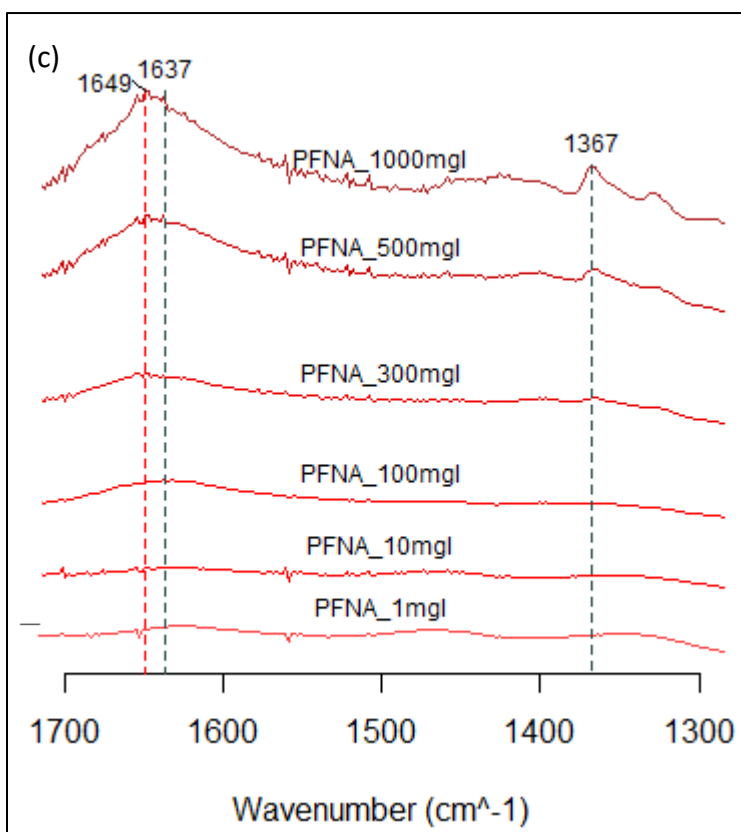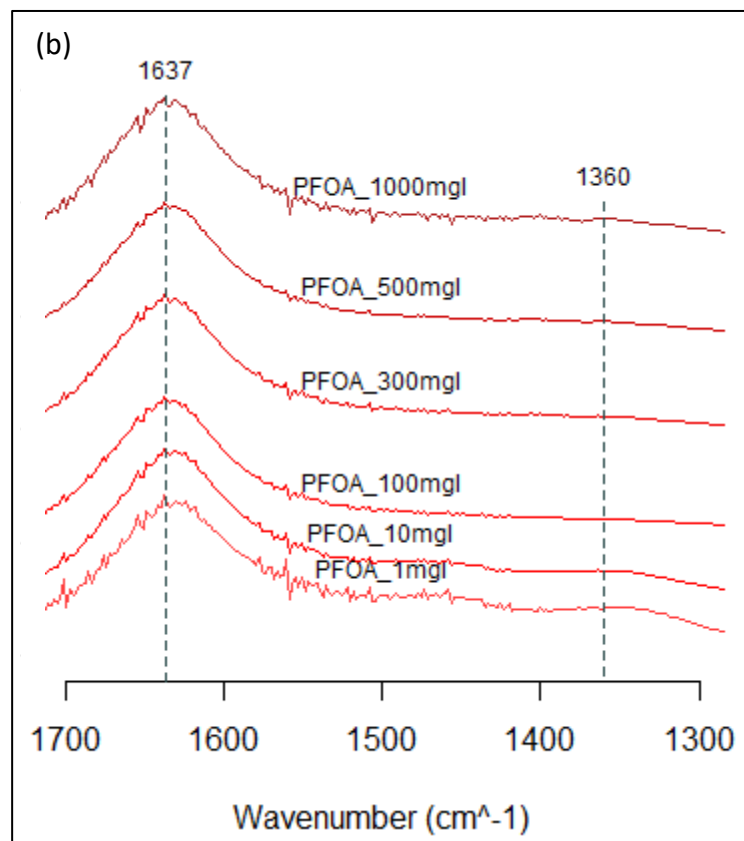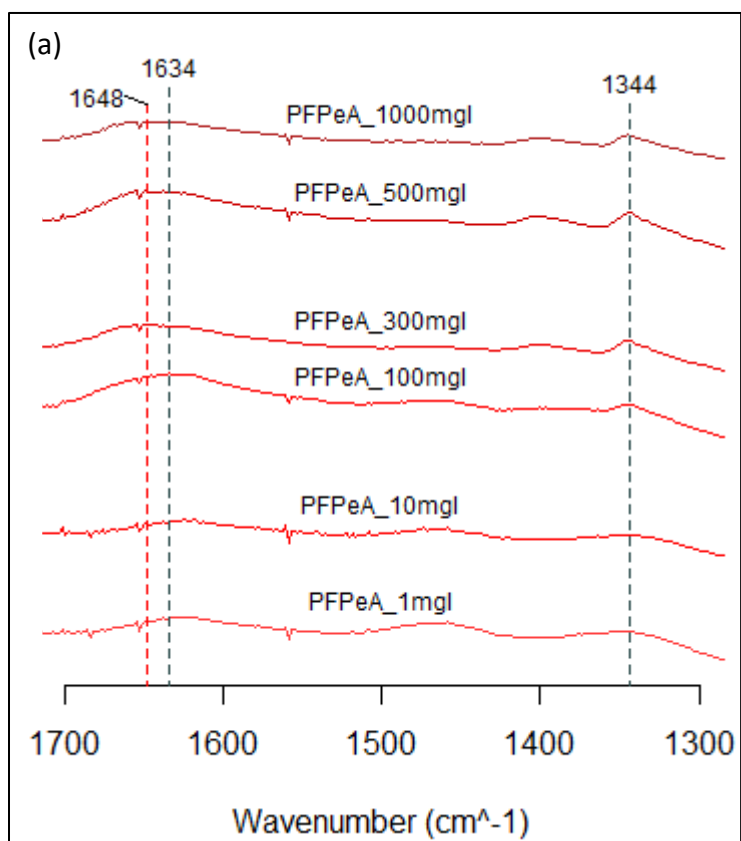
Figure 11: Absorbance spectra in 1700 – 1300 cm⁻¹ carboxylate region of PFCAs at varying loadings. Grey lines mark the smallest possible carboxylate separation (Δ) which is probably only $v_b(H_2O)$ masking the emergence of $v_{as}(COO^-)$. Red lines mark the interpreted band position of $v_{as}(COO^-)$. The spectra are plotted with an offset between eachother for clear visualization, so exact values for absorbance are removed. (a) PFPeA (b) PFOA (c) PFNA (d) PFDA.

26

3.4.3 Sorption isotherms of PFCAs onto ferrihydrite

Figure 12 shows the sorption isotherms of all PFCAs, including the two additional PFOA sample sets with dried sample material and increased amounts of Fh. PFPeA, PFOA and PFNA have increasing concave downward (n < 1) Freundlich isotherms and PFDA a concave
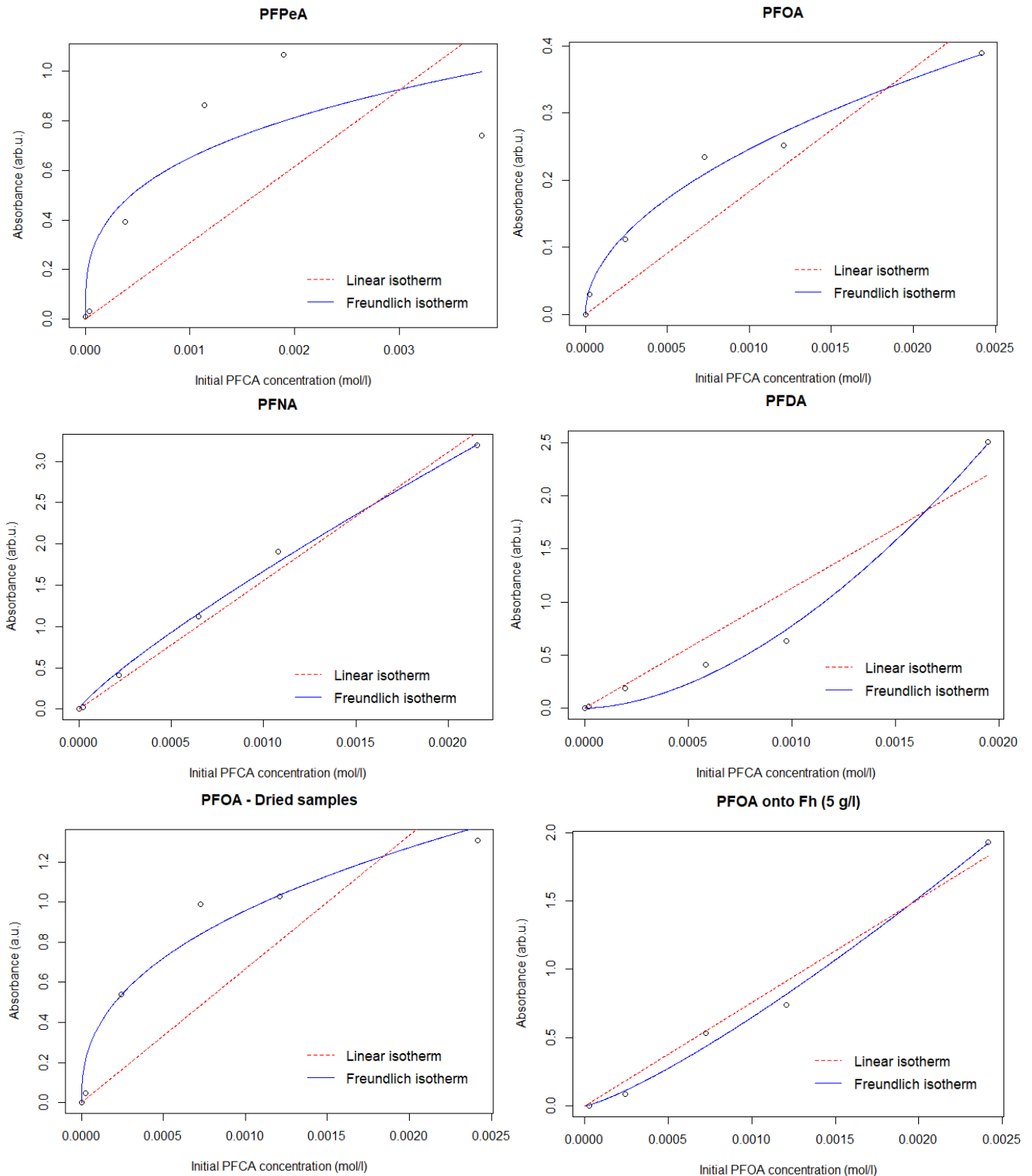
Figure 12: Sorption isotherms of PFCAs onto Fh with both the Freundlich and linear fits made by plotting absorbance of spectra between 1270 – 1110 cm^{-1} vs. initial molar concentration.

upward (n > 1) Freundlich isotherm. PFPeA and PFOA show greatest correspondence with the isotherms fitted on the Freundlich form and are described poorly by the linear forms. PFNAs Freundlich fit exhibits some deviance from a linear shape, but fits reasonably well with both. The sorption isotherm for dried samples of PFOA shows a very similar shape compared to the wet samples, but with a higher absorbance. Sorption samples with an excess amount of Fh (5 g/l) showed a slightly non-linear (n > 1) isotherm, but fits well with a linear relationship. Sorption isotherm parameters for the experiments measured with FTIR used for the modeling in this thesis are in table 7, and parameters from all experimental sets can be found in table B 1.

Table 7: Sorption isotherm parameters obtained from batch reactions with PFCAs and Fh measuring with ATR-FTIR.

| PFCA | Freundlich constants | | Linear |
	K_f	n	K_{Fh}
PFPeA	5.9	0.3201	308
PFOA	8.5	0.5128	183
PFNA	578.8	0.8465	1556
PFDA	142666	1.755	1129.9[a]

[a]K_{Fh} value for PFDA used in the database to generate models for figure 14 and 15.

3.5 SPE-LC-MS/MS

The linear sorption isotherms of aqueous concentration vs. sorbed amounts from LC-MS of PFOA and PFDA (figure 13) yielded logarithmic partition coefficients (Fh-water), log K_{Fh}, of ~2.71 for PFOA and ~4.17 for PFDA. The models were fitted with and without forcing an intercept of 0, and these showed little significant difference in coefficients. Forcing an intercept of 0 is not wrong strictly speaking, as there can be no sorbed amount at an aqueous concentration of 0, but it should not be mistaken for a measured point.
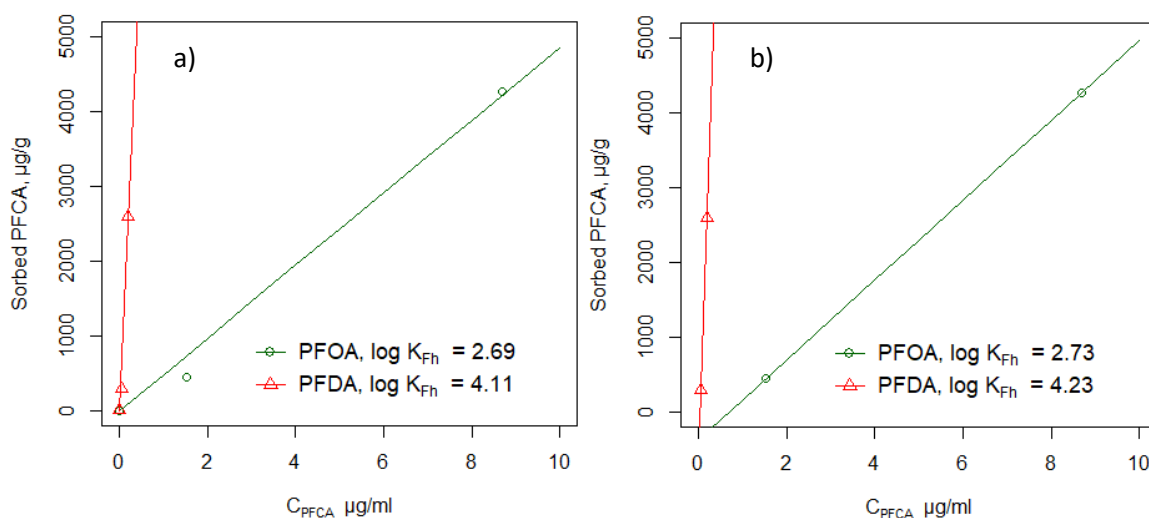
Figure 13: Linear sorption isotherms of PFOA and PFDA from SPE-LC-MS/MS both (a) forcing zero-intercept and (b) not forcing an intercept.

3.6 Transport modeling of PFCAs with PHREEQC

Figure 14 shows simulated aqueous concentrations of PFCAs for a 10 m long simplified Gardermoen aquifer at the last cell i.e. 10 m from the point source. The breakthrough curves of the PFCAs occur in order of PFPeA, PFOA, PFDA and PFNA, where PFDA and PFNA occur approximately at the same time. The first occurrences were after around 1.9, 2 and 3.1 pore volumes corresponding to around 22, 23.1 and 34.7 days, for PFPeA, PFOA, PFNA/PFDA, respectively. After approximately 4 pore volumes or 46.3 days, all PFCAs converge on the initial solution concentrations of 1000 mg/l. At maximum concentrations of PFPeA and PFOA, they are much higher than the initial concentrations and decrease toward 1000 mg/l.
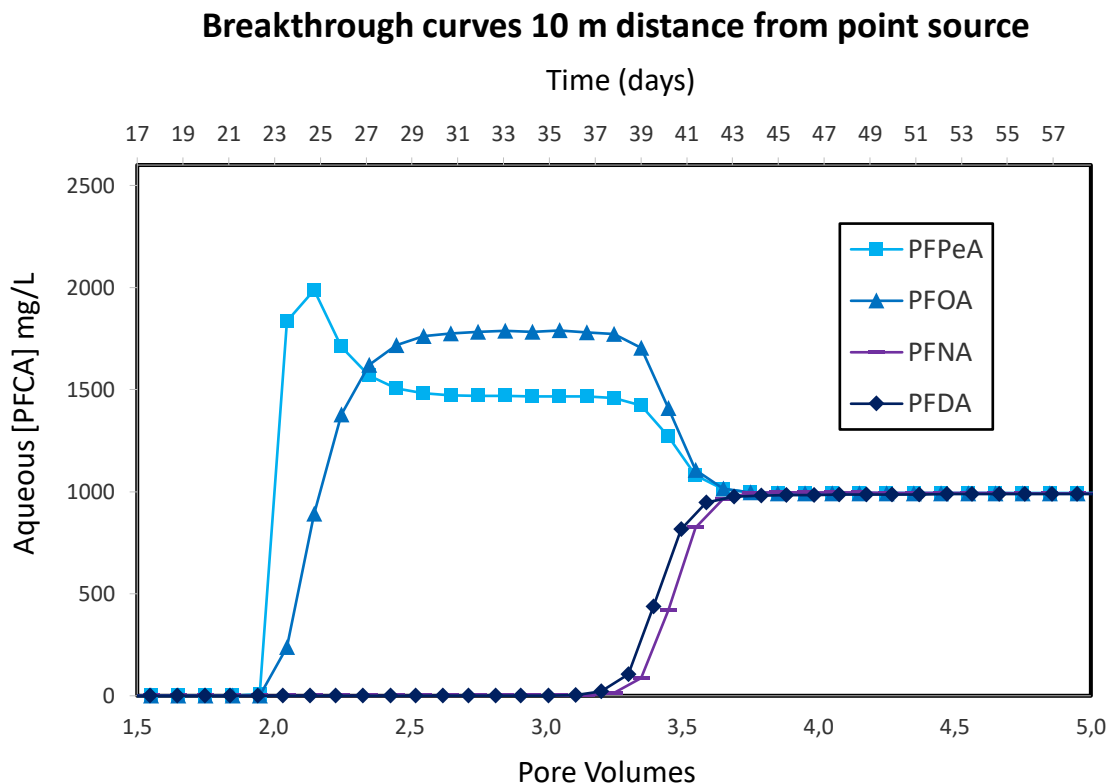
Figure 14: Simulation of aqueous PFCA-concentration at 10 m from point source over time/pore volumes.

Figure 15 shows the same simulation, but with the plotted amounts of sorbed PFCA to Fh. The order of which the PFCAs sorb is the same as the order of first occurrence for aqueous concentrations, and they start to sorb before appearing at significant aqueous concentrations within a day. The equilibrium sorption amount increases by increasing chain length. PFPeA sorption increases to the highest amount of sorption and immediately desorbs in favor of PFOA, both reach equilibrium for a while until a decrease when PFDA and PFNA starts sorbing. At around 4 pore volumes, the defined surfaces and solutions in the aquifer has been equilibrated with all PFCAs. At the final equilibrium, the soil composition of PFCAs are 19 mg/kg, 26 mg/kg, 728 mg/kg and 854 mg/kg for PFPeA, PFOA, PFNA and PFDA, respectively.
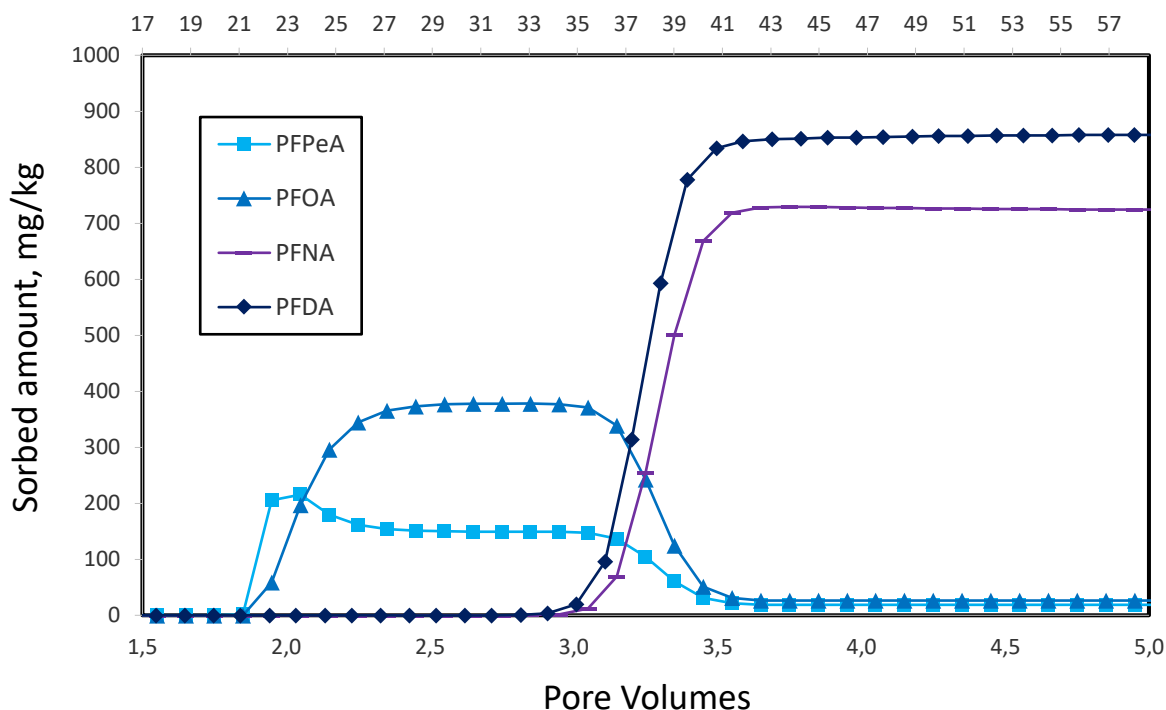
Figure 15: Simulated amounts of sorbed PFCA to Fh 10 m from point source over time/pore volumes.

Modeling by pore volume makes them scalable to any time frame and distance. As an example, breakthrough curves from this model at 1000 m distance from the source would occur after 2200, 2310 and 3470 days for PFPeA, PFOA and PFNA/PFDA, respectively.

4. Discussion

4.1 Analytical uncertainties

4.1.1 Methodology: problems and suggested improvements

There were dissolution issues with the PFCAs, and especially with PFDA. PFPeA was in liquid form and mixed well with water at stock solution concentrations. For the other PFCAs the solids were directly added to water and stirred until no PFCA-crystals or grains were visible. PFDA took several days to seemingly dissolve, although in retrospect it seems unlikely to have fully dissolved. This can explain the apparent lower sorption of PFDA relative to PFNA. There is little information on the pure water solubility of PFDA. Some authors report PFDA saturation in water at ~5 g/l (Kauck and Diesslin, 1951), but there is a lack of literature on the subject. This is attributed to difficulty in attaining true solubility as PFAS tend to produce micellar aggregates at high concentrations, and is the same reason why true pKa of many PFAS has yet to be established (Cabala et al., 2017; Kutsuna et al., 2012). The use of ~100% methanol as the sole solvent for stock solutions of PFAS has not been

uncommon (Kuklenyik et al., 2005; Zhao et al., 2007), but PFCAs are not fully soluble in high purity methanol causing solid phase extraction recoveries of more than 100% when undissolved material was solubilized after addition to aqueous phase samples (Shoemaker et al., 2009). Common practice now is to use a solvent mixture, where a suggested ideal water:methanol solvent ratio for highest sample recovery with SPE-methods was 25:75 (Shoemaker et al., 2009). This would have increased the solubility and concentration accuracy for PFCA stocks in this thesis as well. However, addition of methanol as a solvent could have cluttered IR-spectra giving overlapping absorptions in the CF-, COO-, and OH-region (Socrates, 2001). Methanol in methanol:water solvent will cause preferential solvation of PFOA by methanol even at very small molar fractions (0.045) of methanol (Kutsuna et al., 2012) and does not result in a true sorbent-water equilibrium.

The high PFCA concentrations used in the batch reactions of this thesis will have lowered pH to around the pKa and a significant amount of PFCA should exist in its acid form. Some lower-concentration test runs were done without any apparent absorbance in the CF-region with FTIR and is the reason behind the relatively high concentration batches. This might have been due to the solubility issues instead of a supposed low detection of the ATR-method. A buffer could have been added to control pH to some extent, but could have presented further confounding of IR-spectra.

Polypropylene (PP) flasks are often mentioned as a preferred storage material for PFAS solutions (So et al., 2004; Martin et al., 2004; Kuklenyik et al., 2005), but the claims are seldom substantiated (Point et al., 2019) and PP containers have been shown to be vulnerable to PFAS adsorption as well (Yamashita et al., 2004). Glass and low-density polyethylene (LDPE) are often advised against as PFAS may adsorb, and LDPE may be contaminated with polytetrafluoroethylene (Teflon) from a manufacturing process (So et al., 2004; Martin et al., 2004; MDEQ, 2018). Conversely, Point et al. (2019) found that borosilicate glass containers could increase long chain PFAA recoveries compared to PP. In this thesis it would have been preferred to use PP or HDPE, but there were limitations with laboratory supply.

Overestimation of sorbed PFCA amounts in general can be attributed to uncertainties using absorbance as a proxy for molar concentration. A Lambert-Beer plot is where known concentrations of a substance are measured by an IR-instrument and an absorbance vs. concentration plot is produced, describing the relationship between concentration and absorbance. Converting absorbance to concentration via the Lambert-Beer function from such a plot might reduce some of the overestimation stemming from an unknown molar attenuation coefficient and optical path length, although when measuring on solid phase samples compared to aqueous phases these may vary. It would also improve reproducibility to use fully dried samples to eliminate the chance of high variability in the water content of samples.

4.1.2 XRPD of Fh

The X-rays of interest from a copper anode when using XRD are $K_{\alpha 1}$, $K_{\alpha 2}$ and K_β. "K" denotes the innermost orbital shell of the atom, and the energy difference between the K-shell and higher energy orbitals determine the energy of the emitted X-ray. The energy difference between Cu $K_{\alpha 1}$ and $K_{\alpha 2}$ are so small that they cannot be distinguished with XRD. K_β

however, is a higher energy ray which can be unwanted as it occurs in a smaller proportion of total X-ray light than K_α. A monochromator may filter undesirable radiation of different wavelength, either before sample interaction (primary monochromator) or after (secondary monochromator) (Bunaciu et al., 2015). A copper anode without a monochromator was used for the XRPD of ferrihydrite. Using copper as the X-ray source for detecting crystal structures containing iron is suboptimal. This is because the energy of Cu $K_{\alpha 1}$ (8.047 keV) rays is larger than the absorption edge of iron, Fe K_e (7.112 keV) which ionizes the iron, partly producing fluorescence instead of diffraction (Pecharsky, 2009). This causes a positive intensity shift in the diffractogram and can mask peaks. The raw data had peaks that were not as easily distinguishable compared to the diffractogram in figure 4. Examples of better set-ups for XRD on ferrihydrite are: a copper anode with either a primary or secondary monochromator filtering out Cu K_β rays or X-rays produced by ionized iron, respectively, or better yet would be a cobalt anode with a primary monochromator filtering out Co K_β because Co K_α < Fe K_e, or simply just an iron anode because any K_β of an atom is lower than its K_e (Fransen, 2004; Mos et al., 2018). In all the set-ups described, the monochromators work as band pass filters of radiation. Even with a filter for Cu K_β, the two K_α rays have such similar wavelengths of 1.54 Å and 1.544 Å making them difficult to filter. X-rays with different energies will produce peaks at different band positions, but as the energies of X-rays from the same atom shell are similar, the result is often multiplets or an apparent peak broadening (Pecharsky, 2009). Despite the non-ideal set-up, the result was satisfactory in detecting the characteristic peaks at around 2θ 35° and 62° (Villacís-García et al., 2015; Rout et al., 2012; Vaughan et al., 2012), and since XRD was done to verify the formation of 2-line ferrihydrite and not any of the other more mature iron oxides, it is confidently concluded to be Fh.

The broadness of a peak is inversely proportional to the crystallite size by the Scherrer equation (Scherrer, 1918), and the effect is visible with average crystallite size < 200 nm (Bunaciu et al., 2015). Small crystallites do not necessarily mean small particles as aggregation can lead to significantly larger particles. Low crystallinity gives a low-range structural order and will also contribute to peak broadening, and high porosity leads to lower intensity (Pecharsky, 2009). The broadness of peaks and relatively low intensity of the diffractogram of 2-line Fh is likely caused by a combination of the small average crystallite size, low crystallinity, high porosity and signals from multiple Cu X-rays.

At low Bragg angles the irradiation area of the beam on the sample is at its largest (Pecharsky, 2009). This is usually the cause for an increase in diffractions which is also visible in figure 4, but from 2θ 13-0° there is a sharp break and a decrease in intensity. This is likely due to a surface roughness effect which decreases fluorescence at lower angles in porous samples (Suortti, 1972), and could be exacerbated by poor sample packing.

4.1.3 Problems with the ATR-method

Transmission spectral libraries are most common when comparing spectra which is why ATR-FTIR spectra are corrected. There are some problems related to the ATR-method which already have been mentioned. Regarding penetration depth of a sample, there are several dependent factors, one of which is the refractive index of the sample material which is

unknown. The correction compensates for band intensity loss and peak shifts, both of which are likely somewhat erroneous after corrections have been applied without the real sample refractive index (Nunn and Nishikida, 2008; Grdadolnik, 2002). In the worst case for this thesis, band intensity errors could ultimately lead to wrongful estimation of the absorbance and peak shifts can lead to misjudgments of band assignments.

4.2 ATR-FTIR

4.2.1 Uncertainties of band assignments and interpretations

Condensed phase pure carboxylic acids tend to form dimers where the C=O-group of one acid is hydrogen bonded to the OH-group of another, and vice versa. This creates a packing of a bilayer structure which, in their hydrocarbon counterparts, is responsible for an alternating packing density causing odd and even C-lengths to have lower and higher melting points, respectively (Bond, 2004). A similar bilayer structure with dimeric hydrogen bonded molecules seems to present for PFOA crystals (Omorodion et al., 2018). The observed bands at ~1690 cm^{-1} (figure 8) supports the assertion of hydrogen-bonded C=O for a dimeric structure for all pure condensed phase PFCAs, but is not as visible for PFPeA due to the 1768 cm^{-1} peak (figure 8c). All PFCAs studied here, except PFDA, also exhibit a higher frequency non-hydrogen-bonded C=O band (1768 cm^{-1} and 1754 cm^{-1}) which suggests monomeric carboxylic acids. Monomeric carboxylic acids are characterized by having narrower C=O peaks since hydrogen bonding leads to peak broadening (Kollman and Allen, 1972), and is why it is difficult to conclude to the degree of dimerization. The OH-stretch of a carboxylic acid dimer should yield a large and broad band between frequencies of 3300 – 2700 cm^{-1}, which seems to be present, although at a very low intensity (figure A 1). The more intense and narrower OH-stretch of carboxylic acid monomers at ~3600-3400 cm^{-1} (figure A 2) is further indication of monomeric condensed phase PFCAs. This band falls at the position of v(C=O) overtones, but this is highly unlikely at their intensity (Max and Chapados, 2004). Furthermore, PFDA shows no narrow peak at 1768-1754 cm^{-1}, but does have absorption over 3600-3400 cm^{-1}, and where there are no fundamentals frequencies there can be no overtones. The theoretical spectra (figure A 3) of PFOA show the difference in wavenumber of v(C=O) of the acid monomer (figure A 3a) at higher frequency compared to the dimer (figure A 3b).

The negative absorption peaks around 2365 cm^{-1} visible in the full spectra (figure 16) are due to a decrease in absorption of CO_2 between the time when the background spectrum and the sample were collected (Gerakines et al., 1995).

The carbonate peaks will be present for most solutions close to neutral pH when left to be equilibrated with atmospheric CO_2 pressure. Carbonates typically form hydrogen bonded outer sphere complexes with iron (Bargar et al., 2005) and in figure 11 can be seen to decrease in intensity as PFCA concentration increases which lowers pH. A nitrate peak could also be expected in the samples as the synthetization of Fh requires Fe-nitrate salt (Villacís-García et al., 2015), but is not visible.

In figure 10d, the highest concentration of PFDA show an extremely sharp increase in absorbance intensity as well as narrower peaks. The entire collected spectrum for this sample

33

(figure 16) reveal two peaks around 3400 cm^{-1} and 3540 cm^{-1} related to OH-stretch of carboxylic acids which are not noticeable in any other spectra except for the condensed phase PFCAs. It is likely that this is caused by incomplete dissolution of PFDA. There is also a bump around 1690 cm^{-1} for both 1000 mg/l PFDA and for 1000 mg/l and 500 mg/l PFNA samples which is likely due to a fair amount of PFNA/PFDA being protonated as these acid concentrations give pH lower than, or around, their pKa. PFNA does not have OH-stretch at >3400 cm^{-1} and do not exhibit the same abrupt difference in absorbance as PFDA, but the possibility of dissolution issues for PFNA cannot be excluded.
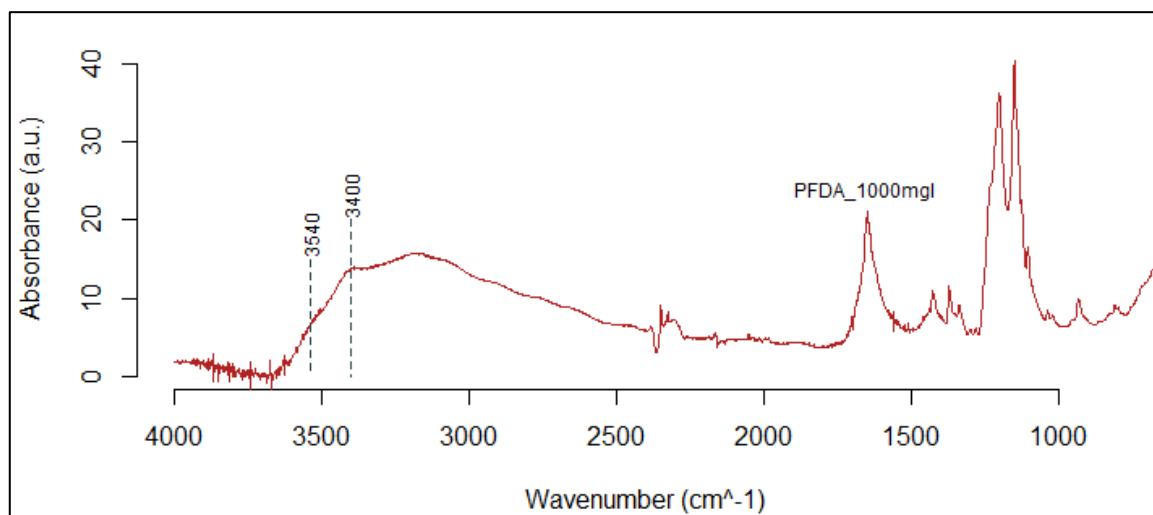

Figure 16: Sorption experiment with PFDA at the highest concentration (1000 mg/l).

4.2.2 Carboxylate region, Δ separation and binding mechanisms

The separation (Δ) in frequency between $v_{as}(COO^-)$ and $v_s(COO^-)$ is used to describe how carboxylic acids bind to metals (Gao and Chorover, 2012; Ha et al., 2008; Zeleňák et al., 2007). The bonding modes of metal-carboxylates follow an order of large to small Δ: unidentate > ionic and bridging bidentate > chelating bidentate corresponding to about Δ 180 cm^{-1} > 160 cm^{-1} >120 cm^{-1}, respectively (Martini et al., 2002; Deacon, 1980; Zeleňák et al., 2007; Nara et al., 1996; Hwang et al., 2007), and Gao and Chorover (2012) found that PFOA bonds by inner sphere sorption as a unidentate ligand to Fe (on nanoparticulate hematite) with Δ ~250 cm^{-1}. From figure 11b, the wet samples of PFOA show the $v_b(H_2O)$, and any water containing samples will have this peak. Samples of the other PFCAs contained less water which is why this peak is not as prominent in these spectra, but it still introduces an issue when interpreting the $v_{as}(COO^-)$ peaks. Another issue lies with the fact that $v(COO^-)$ vary with the degree of hydrogen bonding (Zeleňák et al., 2007), but so does $v_b(H_2O)$ (Chuntonov et al., 2014). However, for higher PFCA concentrations it is expected that the intensity of carboxylate peaks should increase (by Eq. 1) and water intensity should stay approximately constant, and there seems to be a band that emerges at high concentrations around ~1649 cm^{-1} at higher frequency than $v_b(H_2O)$. This is interpreted to be $v_{as}(COO^-)$, and another band at ~1344-1368 cm^{-1} which is likely $v_s(COO^-)$. The theoretical spectrum of the PFOA anion (figure A 3c) shows the $v(COO^-)$ doublet, and also show $v_s(COO^-)$ around 1373 cm^{-1}. The sorption samples show Δ in the range of 281-305 cm^{-1} and supports the assertion of mainly

34

inner sphere sorption by unidentate ligand exchange of PFCAs to iron. Oven dried sorption samples of PFOA can be seen in figure A 4 which show Δ in the same range. Gao and Chorover (2012) proposed a reaction for exchange of protonated surface hydroxyl groups on iron oxide (goethite) with PFOA-anions, here generalized to moieties of $(CF_2)_n$ for n = 3, 6, 7, 8 corresponding to PFCAs of chain length C5, C8, C9, C10:

$$\equiv Fe - OH_2^+ + CF_3(CF_2)_n COO^- \ \rightarrow \ \equiv Fe - OOC(CF_2)_n CF_3 + H_2O$$
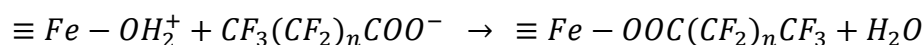
Goethite and Fh share similar surface sites (Hiemstra and Van Riemsdijk, 2009; Hiemstra, 2013; Boily and Song, 2020; Ghose et al., 2010), so it would not be unexpected that surface binding mechanisms are alike.

4.3 Uncertainties in estimated sorption isotherms

4.3.1 Sorption isotherms of PFCAs onto Fh from ATR-FTIR

When the presumed undissolved data for PFDA discussed in the previous section is excluded, all sorption isotherms (figure 12a-c and figure 17), are described well by the Freundlich model. This is in accordance with reported models for sorption of PFCAs to soil (Higgins and Luthy, 2006), and appears similar to PFOS/PFOA sorption on various sorbents like soils (Wei et al., 2017), sand, clay and goethite (Johnson et al., 2007) and activated carbon and biochar (Zhang et al., 2019). Since sorption experiments were run with the same mass concentrations for all PFCAs they will have different molar concentrations. This might be one reason why PFDA and PFNA show a tendency toward linear sorption as there will be less site occupancy on Fh at lower molar concentrations, which could be further lowered if there are solubility issues of long-chain PFCAs in water. It should also be noted that the reported sorption parameters here are not true Freundlich equilibrium constants as they are based on absorbance vs. initial aqueous concentrations. In batch reactions of sorption, when material is sorbed, the aqueous concentrations will be lower than they were initially. If sorption is non-linear with n < 1 the discrepancy between initial and actual aqueous concentrations will be higher at lower initial concentrations.
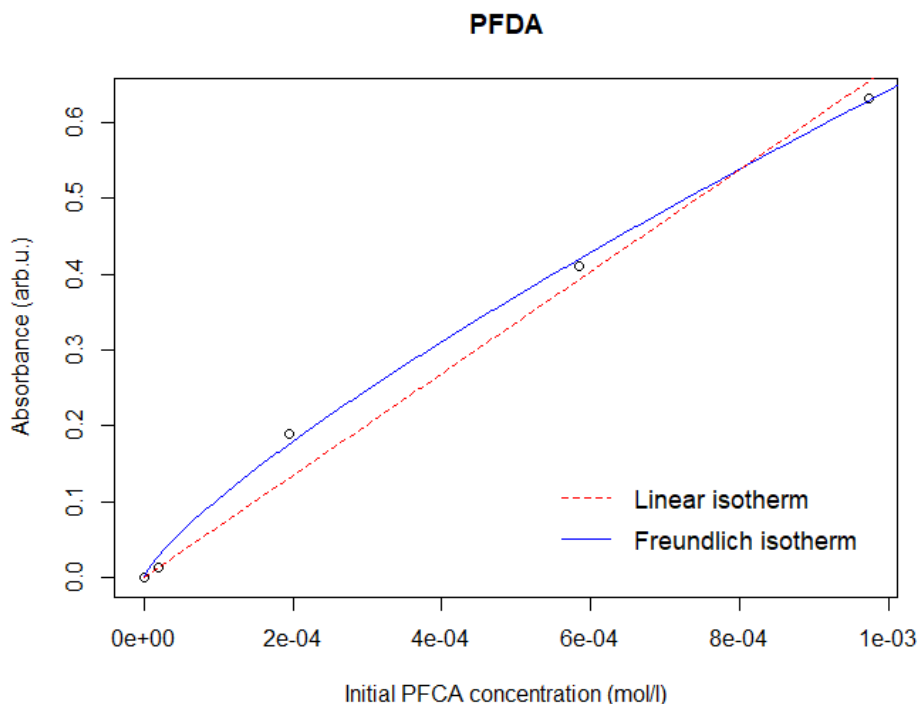
Figure 17: Sorption isotherm of PFDA excluding the undissolved data.

As mentioned in the methods, the sorption sample material was a spreadable wet slurry which was placed directly on the ATR-crystal. The PFOA samples (figure 11b) contained too much water making it difficult to observe peaks relevant for the interpretation of the binding mode, which is why oven dried sorption samples for PFOA were done as well. The Freundlich sorption isotherm of the oven dried samples of PFOA compared to the wet samples have similar n values, but the Freundlich constant, K_f, is double for the dried sample set. When water is removed, especially by evaporation in an oven, it changes the system and is no longer a true Fh-water distribution. PFCAs might protonate and precipitate as concentrations increase by removal of solvent through evaporation, although most supernatant water was removed for the samples before oven drying. The higher K_{Fh}/K_f here is likely due to more sample material on the ATR-crystal. The wet, cohesive, spreadable slurry was more evenly distributed while the dry material formed a thicker, compact layer on the instrument.

An important consequence of determining the type of sorption, for instance linear or non-linear Freundlich sorption, is the difference in how it predicts mobility of a substance. If sorption for a given contaminant is deemed linear when it is in fact Freundlich sorption with n < 1, mobility in the aqueous phase will be underestimated at high concentrations. Often the linear K_d and K_{OC} are cited instead of their non-linear counterparts K_f and K_{fOC}.

36

Table 8: Freundlich and linear partition coefficients for all studied PFCAs.

PFCA	Freundlich constants		Linear
	K_f	n	K_{Fh}
PFPeA	5.9	0.3201	308
PFOA	8.5	0.5128	183
PFNA	578.8	0.8465	1556
PFDA[a]	153	0.7921	673

[a]Coefficients for PFDA are without the undissolved sample data.

The sorption isotherm coefficients for the studied PFCAs can be seen in table 8. PFPeA exhibits the strongest non-linearity of sorption to the point where its K_{Fh} is highly overestimated. To an extent this is true for all PFCAs studied here which is why the non-linear Freundlich model is preferred. Comparing K_f, there is a difference in orders of magnitude between PFPeA/PFOA and PFNA/PFDA. This could be similar to an observed divide where short chain PFCAs (C < 8) were only found in porewater and long chain PFCAs (C > 10) were only found in sediments (Enevoldsen and Juhler, 2010), but PFOA, PFNA and PFDA represent the intermediary range. PFNA has K_f/K_{Fh} several times larger than the other PFCAs. The sorption coefficients are normalized partition coefficients as it is pure Fh, analogous to K_{OC} which is equal to K_d/f_{OC} when OC is assumed to be the primary sorbent in soil. As such, these parameters have to be adjusted for Fh soil content e.g. PFOA in a soil with 1% Fh, the K_d based on parameters from this thesis would be $K_d = K_{Fh} * f_{Fh} = 183 * 0.01 = 1.83$ assuming Fh as the only sorbent.

There are some problems associated with plotting absorbance vs. molar concentrations which have been touched upon earlier in this thesis. Absorbance was normalized to CF-moieties because absorbance/peaks in the CF-region are dependent on how many moieties are present independent of molar concentrations of the concerning molecule, but each moiety's intensity contribution might not be equal. Absorption is related to concentration through Lambert-Beer's law (Eq. 3) as described, but when the molar attenuation coefficient and optical path length are not known, using it as a proxy for concentration becomes a rough approximation. While sorption parameters obtained here cannot be regarded as quantitative, the knowledge lies in the comparison of PFCAs of different chain length.

4.3.2 Sorption isotherms of PFOA and PFDA onto Fh from SPE-LC-MS/MS

As the solid phase of sorption samples were only measured for two concentrations, the resulting sorption isotherms were obviously linear, but the degree of linearity might have been different had more data been available along the entire concentration gradient. The measured aqueous concentrations of PFOA were higher than initial concentrations while PFDA indicated loss of sample material. Issues with measurements from SPE-LC-MS/MS were ascribed to matrix effects or a poor extraction. Due to the high concentrations of the samples, they had to be strongly diluted which also might have influenced results. While exact K_{Fh} values from this method are not accurate, magnitudinal difference between the two PFCAs can be analyzed, and they show a similar relationship where PFDA has a K_{Fh} several times

larger than PFOA, supporting chain-length dependent sorption of perfluorinated compounds on Fh.

4.4 Transport model from the Gardermoen aquifer based on sorption isotherms

The simulated transport model only considers saturated zone groundwater transport with soil-water partitions. As hydrophobic surfactants, a major compartment for environmental contamination with PFAS is the unsaturated zone where they can form reservoirs and exist as a continuous source of groundwater contamination, even up to 20 years after deposition (Weber et al., 2017). The same hydrophobic surfactant properties means PFAS can occur as a non-aqueous phase liquid (NAPL) with other contaminants, like jet fuel (McGuire et al., 2014), which is a likely co-contaminant at fire-fighting practice facilities, and increases sorption when present in low OC soil (Guelfo and Higgins, 2013). The model in this thesis (figure 14 and 15) strictly simulates soil-water equilibrium sorption of PFCAs where the only soil sorbent is Fh and OC content is ignored. The PFCA concentrations in the simulation are higher than what might be considered severely polluted groundwater. The occurrences of PFCAs from the model predicts strong differential transport dependent on chain length. While this is in accordance with other predictive models and observed situations (Brusseau et al., 2019; Weber et al., 2017; Guelfo and Higgins, 2013), some have reported a lack of evidence for chain-length dependent differential groundwater transport (McGuire et al., 2014). It has been suggested that chain-length dependent sorption is not as prominent for short-chain PFCAs due to the hydrophobic effect not being as dominant, and it was hypothesized that ion exchange may play a larger part (Guelfo and Higgins, 2013). This hypothesis offers an explanation for the relatively small gap in observed sorption of PFPeA and PFOA despite the large difference in chain length (C5 vs. C8).

A continuous point source of PFAS contamination might be useful to model in some cases, but it does not take depletion of the contaminant source into account. Another transport model with the same aquifer and contaminant solution composition was simulated (figure B 1), but with an initial pulse of contaminated water to the aquifer and subsequent pumping with clean water. The model simulates three spill scenarios with pulses of 50 L, 20 L and 5 L of contaminated water into the aquifer. Aqueous concentrations of PFCAs are measured at the distance to a recipient (figure B 1). No PFCAs reach the recipient for the 5 L scenario and all PFCAs are sorbed. With a 20 L pulse, only PFPeA and PFOA will reach the recipient since PFNA and PFDA are sorbed. For the 50 L spill, all PFCAs reach the recipient due to the Fh surfaces reaching full sorption capacity.

The models in figure 14, 15 and B 1 uses Freundlich sorption for PFPeA, PFOA and PFNA and linear sorption for PFDA including the possibly undissolved data. Alternative sorption parameters for PFDA excluding undissolved data (table 8) and using Freundlich parameters were used to make the adjusted transport model. A model with these parameters for PFDA will overestimate the relative sorption of PFNA (figure B 2).

Many sorption studies of PFAS consider OC as the sole sorbent in soils and neglect sorption to mineral surfaces. There are indications of increased contribution to PFAS sorption by mineral surfaces and electrostatic interaction when OC content is low (Johnson et al., 2007;

Ahrens et al., 2011; Wei et al., 2017), but even for some lower OC content (0.56 %) soils this contribution is negligible (Higgins and Luthy, 2006). The few studies that exist on the specific sorption of PFOS/PFOA to iron oxides have found significant contributions (PFOA (Gao and Chorover, 2012) and PFOS (Li et al., 2019; Lu et al., 2016; Tang et al., 2010)). Studies on PFCA sorption to iron oxides are sparse, and as PFOA and other PFCAs have become increasingly relevant contaminants in recent years, it is important that regulatory bodies can rely on comprehensive models to determine the distribution in the environment. This thesis provides a first look at sorption of PFOA and PFCAs to ferrihydrite and highlight the need for estimation of sorption parameters to mineral surfaces in low OC content soils.

Conclusion

The separation of carboxylate absorption peaks indicate that PFPeA, PFOA, PFNA and PFDA all bind to iron in 2-line Fh by inner sphere sorption mechanisms. A generalized ligand exchange reaction of PFCAs to Fh is proposed in which $-OH_2^+$ groups bound to $\equiv Fe$ exchanges with PFCA anions to form $\equiv Fe-OOC(CF_2)_nCF_3$.

The IR spectrum of the highest concentration sorption sample with PFDA show signs incomplete dissolution. The highly abrupt increase in absorption and narrowing of peaks along with vibrational frequencies of OH- and carboxylic groups associated with condensed phase PFCAs are indicative of undissolved material. Results of sorption isotherms and parameters are adjusted and undissolved data for PFDA are omitted.

Sorption isotherms of all PFCAs fit well with a non-linear (n < 1) Freundlich equilibrium, but there are obvious differences between sorption of PFPeA and PFOA compared to PFNA and PFDA. PFPeA and PFOA show high degree of non-linearity at n = 0.32 and 0.51, respectively, meaning they will have increased mobility at high concentrations. PFNA and PFDA with n = 0.85 and 0.79, respectively, also show non-linear tendencies, but not to the same degree as for the shorter chain PFCAs. Comparing Freundlich parameter, K_f, between PFPeA and PFOA (5.9 and 8.5) with PFNA and PFDA (578.8 and 153) there is a clear chain length dependence on the degree of sorption. The evidence of chain length dependent sorption is strengthened by the observed linear isotherms, K_{Fh}, of PFOA and PFDA from SPE-LC-MS/MS at 4.85 and 128.8, respectively, although solubility and recovery issues make exact values uncertain. The sorption parameters from batch reaction experiments measured with ATR-FTIR likely overestimates sorption of PFCAs to 2-line Fh due to the use of absorbance as a proxy for concentration.

Model simulations of PFCA transport in the Gardermoen aquifer based on sorption to Fh predicts lower mobility and higher sorption of PFCAs with longer chain length (C > 8). There were solubility issues with PFDA which is likely the cause of its predicted lower sorption compared to PFNA.

A Lambert-Beer plot of known PFCA concentrations could have reduced the overestimated sorption parameters, but introduces other sources of error like variation in optical properties for different materials. The solubility issues could have been improved upon by an organic solvent like methanol, but could have caused unwanted absorbance in IR spectra and would not have been a true sorbent-aqueous equilibrium. HDPE or PP containers should preferably have been used for stock solutions, although there is not a clear consensus of ideal materials when handling PFCAs.

References

3M 1999. Fluorochemical Use, Distribution and Release Overview. Available from
www.regulations.gov Document: EPA-HQ-OPPT-2002-0051-0003.

Ahrens, L., Yeung, L. W. Y., Taniyasu, S., Lam, P. K. S. & Yamashita, N. 2011. Partitioning of
perfluorooctanoate (PFOA), perfluorooctane sulfonate (PFOS) and perfluorooctane
sulfonamide (PFOSA) between water and sediment. *Chemosphere,* 85**,** 731-737.

Ashraf, M. A. 2017. Persistent organic pollutants (POPs): a global issue, a global challenge.
Environmental Science and Pollution Research, 24**,** 4223-4227.

ATSDR 2018. Toxicological Profile for Perfluoroalkyls. U.S. Department of Health and Human Services.
Agency for Toxic Substances and Disease Registry.

Banks, R. E., Smart, B. E. & Tatlow, J. C. 1994. *Organofluorine Chemistry: Principles and Commercial
Applications,* New York, Plenum.

Bargar, J. R., Kubicki, J. D., Reitmeyer, R. & Davis, J. A. 2005. ATR-FTIR spectroscopic characterization
of coexisting carbonate surface complexes on hematite. *Geochimica et cosmochimica acta,*
69**,** 1527-1542.

Beg, M. A. A. & Clark, H. C. 1962. Chemistry of the Trifluoromethyl Group: Part V. Infrared Spectra of
Some Phosphorous Compounds Containing CF$_3$. *Revue canadienne de chimie,* 40**,** 393-398.

Boily, J.-F. & Song, X. 2020. Direct identification of reaction sites on ferrihydrite. *Communications
chemistry,* 3**,** 1-8.

Bond, A. D. 2004. On the crystal structures and melting point alternation of the n-alkyl carboxylic
acids. *New journal of chemistry,* 28**,** 104-114.

Brusseau, M. L., Yan, N., Van Glubt, S., Wang, Y., Chen, W., Lyu, Y., Dungan, B., Carroll, K. C. &
Holguin, F. O. 2019. Comprehensive retention model for PFAS transport in subsurface
systems. *Water research,* 148**,** 41-50.

Buck, R. C., Franklin, J., Berger, U., Conder, J. M., Cousins, I. T., De Voogt, P., Jensen, A. A., Kannan, K.,
Mabury, S. A. & Van Leeuwen, S. P. 2011. Perfluoroalkyl and polyfluoroalkyl substances in the
environment: Terminology, classification, and origins. *Integrated Environmental Assessment
and Management,* 7**,** 513-541.

Bunaciu, A. A., UdriŞTioiu, E. & Aboul-Enein, H. 2015. X-Ray Diffraction: Instrumentation and
Applications. *Critical reviews in analytical chemistry / CRC,* 45.

Bunn, C. W. & Howells, E. R. 1954. Structures of Molecules and Crystals of Fluoro-Carbons. *Nature,*
174**,** 549-551.

Butenhoff, J. L., Kennedy, G. L., Frame, S. R., O'Connor, J. C. & York, R. G. 2004. The reproductive
toxicology of ammonium perfluorooctanoate (APFO) in the rat. *Toxicology,* 196**,** 95-116.

Cabala, R., Nesmerak, K. & Vlasakova, T. 2017. Dissociation constants of perfluoroalkanoic acids.
Monatshefte für Chemie - Chemical Monthly, 148**,** 1679-1684.

Cabaniss, S. E. & McVey, I. F. 1995. Aqueous infrared carboxylate absorbances: aliphatic
monocarboxylates. *Spectrochimica acta. Part A, Molecular and biomolecular spectroscopy,*
51**,** 2385-2395.

Chuntonov, L., Kumar, R. & Kuroda, D. G. 2014. Non-linear infrared spectroscopy of the water
bending mode: direct experimental evidence of hydration shell reorganization? *Physical
chemistry chemical physics : PCCP,* 16**,** 13172-13181.

Coates, J. 2006. Interpretation of Infrared Spectra, A Practical Approach.

Conder, J. M., Hoke, R. A., Wolf, W. d., Russell, M. H. & Buck, R. C. 2008. Are PFCAs Bioaccumulative?
A Critical Review and Comparison with Regulatory Criteria and Persistent Lipophilic
Compounds. *Environ. Sci. Technol,* 42**,** 995-1003.

Cormanich, R. A., Hagan, D. & Bühl, M. 2017. Hyperconjugation Is the Source of Helicity in
Perfluorinated n-Alkanes. *Angew Chem Int Ed Engl,* 56**,** 7867-7870.

Danilczuk, M., Lin, L., Schlick, S., Hamrock, S. J. & Schaberg, M. S. 2011. Understanding the fingerprint
region in the infra-red spectra of perfluorinated ionomer membranes and corresponding

model compounds: Experiments and theoretical calculations. *Journal of power sources,* 196**,** 8216-8224.

Deacon, G. 1980. Relationships between the carbon-oxygen stretching frequencies of carboxylato complexes and the type of carboxylate coordination. *Coordination chemistry reviews,* 33**,** 227-250.

Ding, G. & Peijnenburg, W. 2013. Physicochemical Properties and Aquatic Toxicity of Poly- and Perfluorinated Compounds. *Critical Reviews in Environmental Science and Technology,* 43**,** 598-678.

Dzombak, D. A. & Morel, F. M. Surface Complexation Modeling: Hydrous Ferric Oxide. 1990.

Döbelin, N. & Kleeberg, R. 2015. Profex : a graphical user interface for the Rietveld refinement program BGMN. *J Appl Crystallogr,* 48**,** 1573-1580.

Enevoldsen, R. & Juhler, R. 2010. Perfluorinated compounds (PFCs) in groundwater and aqueous soil extracts: using inline SPE-LC-MS/MS for screening and sorption characterisation of perfluorooctane sulphonate and related compounds. *Analytical and Bioanalytical Chemistry,* 398**,** 1161-1172.

European Environment Agency. 2019. *Emerging chemical risks in Europe - 'PFAS'* [Online]. Available: https://www.eea.europa.eu/themes/human/chemicals/emerging-chemical-risks-in-europe [Accessed 01.05.2020].

European Union 2006. Official Journal of the European Union. *L 209,* Volume 49.

Fransen, M. J. 1- and 2-Dimensional Detection Systems and the Problem of Sample Fluorescence in X-ray Diffractometry. 2004.

Frisch, M. J., Trucks, G. W., Schlegel, H. B., Scuseria, G. E., Robb, M. A., Cheeseman, J. R., Scalmani, G., Barone, V., Mennucci, B., Petersson, G. A., Nakatsuji, H., Caricato, M., Li, X., Hratchian, H. P., Izmaylov, A. F., Bloino, J., Zheng, G., Sonnenberg, J. L., Hada, M., Ehara, M., Toyota, K., Fukuda, R., Hasegawa, J., Ishida, M., Nakajima, T., Honda, Y., Kitao, O., Nakai, H., Vreven, T., Montgomery, J. A. J., Peralta, J. E., Ogliaro, F., Bearpark, M., Heyd, J. J., Brothers, E., Kudin, K. N., Staroverov, V. N., Kobayashi, R., Normand, J., Raghavachari, K., Rendell, A., Burant, J. C., Iyengar, S. S., Tomasi, J., Cossi, M., Rega, N., Millam, N. J., Klene, M., Knox, J. E., Cross, J. B., Bakken, V., Adamo, C., Jaramillo, J., Gomperts, R., Stratmann, R. E., Yazyev, O., Austin, A. J., Cammi, R., Pomelli, C., Ochterski, J. W., Martin, R. L., Morokuma, K., Zakrzewski, V. G., Voth, G. A., Salvador, P., Dannenberg, J. J., Dapprich, S., Daniels, A. D., Farkas, Ö., Foresman, J. B., Ortiz, J. V., Cioslowski, J. & Fox, D. J. 2010. Gaussian 09. Wallingford CT: Gaussian Inc.

Fromme, H., Tittlemier, S. A., Völkel, W., Wilhelm, M. & Twardella, D. 2009. Perfluorinated compounds – Exposure assessment for the general population in western countries. *International Journal of Hygiene and Environmental Health,* 212**,** 239-270.

Gao, X. & Chorover, J. 2012. Adsorption of perfluorooctanoic acid and perfluorooctanesulfonic acid to iron oxide surfaces as studied by flow-through ATR-FTIR spectroscopy. *Environmental Chemistry,* 9**,** 148.

Gerakines, P. A., Schutte, W. A., Greenberg, J. M. & Dishoeck, E. F. v. 1995. The infrared band strengths of H2O, CO and CO2 in laboratory simulations of astrophysical ice mixtures.

Ghose, S. K., Waychunas, G. A., Trainor, T. P. & Eng, P. J. 2010. Hydrated goethite (α-FeOOH) (100) interface structure: Ordered water and surface functional groups. *Geochimica et Cosmochimica Acta,* 74**,** 1943-1953.

Goldstein, J. I., Newbury, D. E., Michael, J. R., Ritchie, N. W. M., Scott, J. H. J. & Joy, D. C. 2017. *Scanning Electron Microscopy and X-Ray Microanalysis,* New York, NY, New York, NY: Springer.

Grdadolnik, J. 2002. ATR-FTIR spectroscopy: Its advantages and limitations. *Acta Chimica Slovenica,* 49**,** 631-642.

Guelfo, J. L. & Higgins, C. P. 2013. Subsurface Transport Potential of Perfluoroalkyl Acids at Aqueous Film-Forming Foam (AFFF)-Impacted Sites. *Environ. Sci. Technol,* 47**,** 4164-4171.

Ha, J., Hyun Yoon, T., Wang, Y., Musgrave, C. B. & Brown, J. G. E. 2008. Adsorption of Organic Matter at Mineral/Water Interfaces: 7. ATR-FTIR and Quantum Chemical Study of Lactate Interactions with Hematite Nanoparticles. *Langmuir,* 24**,** 6683-6692.

Hagan, D. 2008. Understanding organofluorine chemistry. An introduction to the C–F bond. *Chem Soc Rev,* 37**,** 308-319.

Hanson, B. A. 2020. ChemoSpec: Exploratory Chemometrics for Spectroscopy.

Hiemstra, T. 2013. Surface and mineral structure of ferrihydrite. *Geochimica et cosmochimica acta,* 105**,** 316-325.

Hiemstra, T. & Van Riemsdijk, W. H. 2009. A surface structural model for ferrihydrite I: Sites related to primary charge, molar mass, and mass density. *Geochimica et Cosmochimica Acta,* 73**,** 4423-4436.

Higgins, C. P. & Luthy, R. G. 2006. Sorption of Perfluorinated Surfactants on Sediments †. *Environmental Science & Technology,* 40**,** 7251-7256.

Huang, S. & Jaffé, P. R. 2019. Defluorination of Perfluorooctanoic Acid (PFOA) and Perfluorooctane Sulfonate (PFOS) by Acidimicrobium sp. Strain A6. *Environ. Sci. Technol,* 53**,** 11410-11419.

Hwang, Y. S., Liu, J., Lenhart, J. J. & Hadad, C. M. 2007. Surface complexes of phthalic acid at the hematite/water interface. *J Colloid Interface Sci,* 307**,** 124-134.

International Ski Federation. 2019. Available: https://www.fis-ski.com/en/international-ski-federation/news-multimedia/news/decisions-of-the-fis-council-meeting-in-constance-ger-autumn-2019 [Accessed 29.04.2020].

Jang, S. S., Blanco, M., Goddard, W. A., Caldwell, G. & Ross, R. B. 2003. The Source of Helicity in Perfluorinated N-Alkanes. *Macromolecules,* 36**,** 5331-5341.

Johnson, R. L., Anschutz, A. J., Smolen, J. M., Simcik, M. F. & Penn, R. L. 2007. The Adsorption of Perfluorooctane Sulfonate onto Sand, Clay, and Iron Oxide Surfaces. *Journal of Chemical & Engineering Data,* 52**,** 1165-1170.

Kannan, K., Corsolini, S., Falandysz, J., Fillmann, G., Kumar, K. S., Loganathan, B. G., Mohd, M. A., Olivero, J., Wouwe, N. V., Yang, J. H. & Aldous, K. M. 2004. Perfluorooctanesulfonate and Related Fluorochemicals in Human Blood from Several Countries. *Environ. Sci. Technol,* 38**,** 4489-4495.

Kauck, E. A. & Diesslin, A. R. 1951. Some Properties of Perfluorocarboxylic Acids. *Industrial & Engineering Chemistry,* 43**,** 2332-2334.

Kissa, E. 2001. Fluorinated Surfactants and Repellents. *Textile Research Journal,* 71**,** 750c-750c.

Kłonowski, M., Breedveld, G. & Aagaard, P. 2008. Spatial and Temporal Changes of Jet Fuel Contamination in an Unconfined Sandy Aquifer. *An International Journal of Environmental Pollution,* 188**,** 9-30.

Knudsen, J. B. S. 2003. *Reactive transport of dissolved aromatic compounds under oxygen limiting conditions in sandy aquifer sediments.* no. 289, Department of Geology, Faculty of Mathematics and Natural Sciences, University of Oslo Unipub.

Kollman, P. A. & Allen, L. C. 1972. Theory of the hydrogen bond. *Chemical Reviews,* 72**,** 283-303.

Komatina, M. M. 2004. Chapter 4 - Anthropogenic Factors. *In:* KOMATINA, M. M. (ed.) *Developments in Earth and Environmental Sciences.* Elsevier.

Kuklenyik, Z., Needham, L. L. & Calafat, A. M. 2005. Measurement of 18 Perfluorinated Organic Acids and Amides in Human Serum Using On-Line Solid-Phase Extraction. *Anal. Chem,* 77**,** 6085-6091.

Kunieda, H. & Shinoda, K. 1976. Krafft points, critical micelle concentrations, surface tension, and solubilizing power of aqueous solutions of fluorinated surfactants. *J. Phys. Chem,* 80**,** 2468-2470.

Kutsuna, S., Hori, H., Sonoda, T., Iwakami, T. & Wakisaka, A. 2012. Preferential solvation of perfluorooctanoic acid (PFOA) by methanol in methanol–water mixtures: A potential overestimation of the dissociation constant of PFOA using a Yasuda–Shedlovsky plot. *Atmospheric Environment,* 49**,** 411-414.

La Mesa, C. & Sesta, B. 1987. Micelles in perfluorinated surfactant solutions. *The Journal of Physical Chemistry,* 91**,** 1450-1454.

Larkin, P. 2011a. Chapter 2 - Basic Principles. *Infrared and Raman Spectroscopy: Principles and Spectral Interpretation.* Elsevier Inc.

Larkin, P. 2011b. Chapter 3 - Instrumentation and Sampling Methods. *Infrared and Raman Spectroscopy: Principles and Spectral Interpretation.* Elsevier Inc.

Larkin, P. 2011c. Chapter 6 - IR and Raman Spectra-Structure Correlations: Characteristic Group Frequencies. *In:* LARKIN, P. (ed.) *Infrared and Raman Spectroscopy: Principles and Spectral Interpretation.* Oxford: Elsevier Inc.

Larkin, P. 2011d. Chapter 7 - General Outline and Strategies for IR and Raman Spectral Interpretation. *Infrared and Raman Spectroscopy: Principles and Spectral Interpretation.* Elsevier Inc.

Lau, C., Thibodeaux, J. R., Hanson, R. G., Narotsky, M. G., Rogers, J. M., Lindstrom, A. B. & Strynar, M. J. 2006. Effects of Perfluorooctanoic Acid Exposure during Pregnancy in the Mouse. *Toxicol Sci,* 90**,** 510-518.

Li, K., Wang, P., Qian, J., Wang, C., Xing, L., Liu, J., Tian, X., Lu, B. & Tang, W. 2019. Effects of sediment components and TiO2 nanoparticles on perfluorooctane sulfonate adsorption properties. *Journal of Soils and Sediments,* 19**,** 2034-2047.

Liu, J. & Mejia Avendaño, S. 2013. Microbial degradation of polyfluoroalkyl chemicals in the environment: A review. *Environment International,* 61**,** 98-114.

Lu, X., Deng, S., Wang, B., Huang, J., Wang, Y. & Yu, G. 2016. Adsorption behavior and mechanism of perfluorooctane sulfonate on nanosized inorganic oxides. *Journal of Colloid And Interface Science,* 474**,** 199-205.

Manceau, A. & Drits, V. A. 1993. Local Structure of Ferrihydrite and Feroxyhite by Exafs Spectroscopy. *Clay Minerals,* 28**,** 165-184.

Martin, J. W., Kannan, K., Berger, U., de Voogt, P., Field, J., Franklin, J., Giesy, J. P., Harner, T., Muir, D. C. G., Scott, B., Kaiser, M., Järnberg, U., Jones, K. C., Mabury, S. A., Schroeder, H., Simcik, M., Sottani, C., van Bavel, B., Kärrman, A., Lindström, G. & van Leeuwen, S. 2004. Analytical challenges hamper perfluoroalkyl research. *Environ Sci Technol,* 38**,** 248A.

Martin, J. W., Mabury, S. A., Solomon, K. R. & Muir, D. C. G. 2003. Bioconcentration and tissue distribution of perfluorinated acids in rainbow trout (Oncorhynchus mykiss). *Environ Toxicol Chem,* 22**,** 196-204.

Martini, D., Pellei, M., Pettinari, C., Skelton, B. W. & White, A. H. 2002. Synthesis, spectroscopic and structural characterization of Cu(II) derivatives of tris(pyrazol-1-yl)methanes. *Inorganica Chimica Acta,* 333**,** 72-82.

Max, J.-J. & Chapados, C. 2004. Infrared Spectroscopy of Aqueous Carboxylic Acids: Comparison between Different Acids and Their Salts. *J. Phys. Chem. A,* 108**,** 3324-3337.

Max, J.-J. & Chapados, C. 2009. Isotope effects in liquid water by infrared spectroscopy. III. H2O and D2O spectra from 6000 to 0 cm(-1). *J Chem Phys,* 131**,** 184505.

McGuire, M. E., Schaefer, C., Richards, T., Backe, W. J., Field, J. A., Houtz, E., Sedlak, D. L., Guelfo, J. L., Wunsch, A. & Higgins, C. P. 2014. Evidence of Remediation-Induced Alteration of Subsurface Poly- and Perfluoroalkyl Substance Distribution at a Former Firefighter Training Area. *Environ. Sci. Technol,* 48**,** 6644-6652.

MDEQ 2018. General PFAS Sampling Guidance. *In:* QUALITY, M. D. O. E. (ed.).

Milinovic, J., Lacorte, S., Vidal, M. & Rigol, A. 2015. Sorption behaviour of perfluoroalkyl substances in soils. *Sci Total Environ,* 511**,** 63-71.

Mos, Y. M., Vermeulen, A. C., Buisman, C. J. N. & Weijma, J. 2018. X-Ray Diffraction of Iron Containing Samples: The Importance of a Suitable Configuration. *Geomicrobiology journal,* 35**,** 511-517.

Müller, C. E., De Silva, A. O., Small, J., Williamson, M., Wang, X., Morris, A., Katz, S., Gamberg, M. & Muir, D. C. G. 2011. Biomagnification of Perfluorinated Compounds in a Remote Terrestrial Food Chain: Lichen–Caribou–Wolf. *Environ. Sci. Technol,* 45**,** 8665-8673.

Nara, M., Torii, H. & Tasumi, M. 1996. Correlation between the Vibrational Frequencies of the Carboxylate Group and the Types of Its Coordination to a Metal Ion: An ab Initio Molecular Orbital Study. *J. Phys. Chem,* 100**,** 19812-19817.

Norwegian Institute for Air Research 2019. Screening new PFAS compunds 2018. ***NILU report 23/2019****.*

Norwegian Pollution Control Authority 2008. Screening of Polyfluorinated Organic Compounds at Four Fire Training Facilities in Norway.

Nunn, S. & Nishikida, K. 2008. Advanced ATR Correction Algorithm. *Application Note: 50581.* Madison, Wisconcsin, USA: Thermo Fisher Scientific.

Omorodion, H., Palenzuela, M., Ruether, M., Twamley, B., Platts, J. A. & Baker, R. J. 2018. A rationally designed perfluorinated host for the extraction of PFOA from water utilising non-covalent interactions. *New journal of chemistry,* 42**,** 7956-7968.

Parkhurst, D. L. & Appelo, C. A. J. 2013. *Description of Input and Examples for PHREEQC Version 3--A Computer Program for Speciation, Batch-Reaction, One-Dimensional Transport, and Inverse Geochemical Calculations*.

Parsons, J., Saez, M., Dolfing, J. & De Voogt, P. 2008. Biodegradation of Perfluorinated Compounds. *Reviews of environmental contamination and toxicology,* 196**,** 53-71.

Pecharsky, V. K. 2009. Fundamentals of Powder Diffraction and Structural Characterization of Materials. *In:* ZAVALIJ, P. Y. (ed.) 2nd ed. ed. Boston, MA: Springer US.

PHE 2009. PFOS and PFOA: Toxicological Overview (Version 1). Toxicology Department. Public Health England.

Point, A. D., Holsen, T. M., Fernando, S., Hopke, P. K. & Crimmins, B. S. 2019. Towards the development of a standardized method for extraction and analysis of PFAS in biological tissues. *Environmental science water research & technology,* 5**,** 1876-1886.

Prevedouros, K., Cousins, I. T., Buck, R. C. & Korzeniowski, S. H. 2006. Sources, Fate and Transport of Perfluorocarboxylates. *Environmental Science & Technology,* 40**,** 32-44.

R Core Team 2020. R: A language and environment for statistical computing. Vienna, Austria: R Foundation for Statistical Computing.

Rout, K., Mohapatra, M. & Anand, S. 2012. 2-Line ferrihydrite: synthesis, characterization and its adsorption behaviour for removal of Pb(ii), Cd(ii), Cu(ii) and Zn(ii) from aqueous solutions. *Dalton Trans,* 41**,** 3302.

Scheringer, M., Strempel, S., Hukari, S., Ng, C. A., Blepp, M. & Hungerbuhler, K. 2012. How many persistent organic pollutants should we expect? *Atmospheric Pollution Research,* 3**,** 383-391.

Scherrer, P. 1918. Bestimmung der Grösse und der inneren Struktur von Kolloidteilchen mittels Röntgenstrahlen. *Nachrichten von der Gesellschaft der Wissenschaften zu Göttingen, Mathematisch-Physikalische Klasse,* 2**,** 98-100.

Schwertmann, U. 1991. *Iron oxides in the laboratory : preparation and characterization,* Weinheim, VCH.

Scott, B. F., Moody, C. A., Spencer, C., Small, J. M., Muir, D. C. G. & Mabury, S. A. 2006. Analysis for Perfluorocarboxylic Acids/Anions in Surface Waters and Precipitation Using GC–MS and Analysis of PFOA from Large-Volume Samples. *Environmental Science & Technology,* 40**,** 6405-6410.

Secretariat of the Stockholm Convention (SSC) 2018. Stockholm Convention on Persistent Organic Pollutants (POPs): Texts and Annexes.

Shipman, S. T., Douglass, P. C., Yoo, H. S., Hinkle, C. E., Mierzejewski, E. L. & Pate, B. H. 2007. Vibrational dynamics of carboxylic acid dimers in gas and dilute solution. *Phys Chem Chem Phys,* 9**,** 4572.

Shoemaker, J. & Tettenhorst, D. 2020. Method 537.1 Determination of Selected Per- and Polyflourinated Alkyl Substances in Drinking Water by Solid Phase Extraction and Liquid Chromatography/Tandem Mass Spectrometry (LC/MS/MS). Washington, DC: U.S. Environmental Protection Agency.

Shoemaker, J. A., Boutin, B. & Grimmett, P. 2009. Development of a U.S. EPA drinking water method for the analysis of selected perfluoroalkyl acids by solid-phase extraction and LC-MS-MS. *J Chromatogr Sci,* 47**,** 3-11.

Siegemund, G., Schwertfeger, W., Feiring, A., Smart, B., Behr, F., Vogel, H. & McKusick, B. 2000. Fluorine Compounds, Organic. *Ullmann's Encyclopedia of Industrial Chemistry*.

Simister, E. A., Lee, E. M., Lu, J. R., Thomas, R. K., Ottewill, R. H., Rennie, A. R. & Penfold, J. 1992. Adsorption of ammonium perfluorooctanoate and ammonium decanoate at the air/solution interface. *Journal of the Chemical Society. Faraday transactions,* 88**,** 3033.

So, M. K., Taniyasu, S., Yamashita, N., Giesy, J. P., Zheng, J., Fang, Z., Im, S. H. & Lam, P. K. S. 2004. Perfluorinated Compounds in Coastal Waters of Hong Kong, South China, and Korea. *Environ. Sci. Technol,* 38**,** 4056-4063.

Socrates, G. 2001. *Infrared and Raman characteristic group frequencies : tables and charts,* Chichester, Wiley.

Stahl, T., Falk, S., Failing, K., Berger, J., Georgii, S. & Brunn, H. 2012. Perfluorooctanoic Acid and Perfluorooctane Sulfonate in Liver and Muscle Tissue from Wild Boar in Hesse, Germany. *Arch Environ Contam Toxicol,* 62**,** 696-703.

Stahl, T., Mattern, D. & Brunn, H. 2011. Toxicology of perfluorinated compounds. *Environmental sciences Europe,* 23**,** 1-52.

Statistics Norway (SSB). 2019. *Arealbruk og arealressurser* [Online]. Available: https://www.ssb.no/natur-og-miljo/statistikker/arealstat/aar [Accessed 30.04.2020].

Steinle-Darling, E. & Reinhard, M. 2008. Nanofiltration for Trace Organic Contaminant Removal: Structure, Solution, and Membrane Fouling Effects on the Rejection of Perfluorochemicals. *Environ. Sci. Technol,* 42**,** 5292-5297.

Stockholm Convention 2009. SC-4/17: Listing of perfluorooctane sulfonic acid, its salts and perfluorooctane sulfonyl fluoride.

Stockholm Convention 2019. SC-9/12: Listing of perfluorooctanoic acid (PFOA), its salts and PFOA-related compounds.

Suortti, P. 1972. Effects of porosity and surface roughness on the X-ray intensity reflected from a powder specimen. *Journal of Applied Crystallography,* 5**,** 325-331.

Søvik, A. K. & Aagaard, P. 2003. Spatial variability of a solid porous framework with regard to chemical and physical properties. *Geoderma,* 113**,** 47-76.

Tang, C. Y., Shiang Fu, Q., Gao, D., Criddle, C. S. & Leckie, J. O. 2010. Effect of solution chemistry on the adsorption of perfluorooctane sulfonate onto mineral surfaces. *Water Research,* 44**,** 2654-2662.

UNEP 2006. Risk Profile on Perfluorooctane Sulfonate. Geneva: United Nations Environment Programme. Stockholm Convention of Persistent Organic Pollutants Review Committee.

vanLoon, G. W. & Duffy, S. J. 2017. *Environmental Chemistry : A Global Perspective,* Oxford, Oxford University Press.

Vargas, C., Song, B., Camps, M. & Häggblom, M. M. 2000. Anaerobic degradation of fluorinated aromatic compounds. *Appl Microbiol Biotechnol,* 53**,** 342-347.

Vaughan, G., Brydson, R. & Brown, A. 2012. Characterisation of Synthetic Two-line Ferrihydrite by Electron Energy Loss Spectroscopy. *Journal of physics. Conference series,* 371**,** 12079.

Villacís-García, M., Ugalde-Arzate, M., Vaca-Escobar, K., Villalobos, M., Zanella, R. & Martínez-Villegas, N. 2015. Laboratory synthesis of goethite and ferrihydrite of controlled particle sizes. *Boletín de la Sociedad Geológica Mexicana,* 67**,** 433-446.

Villalobos, M. & Antelo, J. 2011. A Unified Surface Structural Model for Ferrihydrite: Proton Charge, Electrolyte Binding, and Arsenate Adsorption. *Revista Internacional de Contaminacion Ambiental,* 27**,** 139-151.

Weber, A. K., Barber, L. B., LeBlanc, D. R., Sunderland, E. M. & Vecitis, C. D. 2017. Geochemical and Hydrologic Factors Controlling Subsurface Transport of Poly- and Perfluoroalkyl Substances, Cape Cod, Massachusetts. *Environ. Sci. Technol,* 51**,** 4269-4279.

Wei, C., Song, X., Wang, Q. & Hu, Z. 2017. Sorption kinetics, isotherms and mechanisms of PFOS on soils with different physicochemical properties. *Ecotoxicology and Environmental Safety,* 142**,** 40-50.

Wiberg, K. B. & Rablen, P. R. 1993. Origin of the stability of carbon tetrafluoride: negative hyperconjugation reexamined. *Journal of the American Chemical Society,* 115**,** 614-625.

Yamashita, N., Kannan, K., Taniyasu, S., Horii, Y., Okazawa, T., Petrick, G. & Gamo, T. 2004. Analysis of Perfluorinated Acids at Parts-Per-Quadrillion Levels in Seawater Using Liquid Chromatography-Tandem Mass Spectrometry. *Environ. Sci. Technol,* 38**,** 5522-5528.

Zeleňák, V., Vargová, Z. & Györyová, K. 2007. Correlation of infrared spectra of zinc(II) carboxylates with their structures. *Spectrochim Acta A Mol Biomol Spectrosc,* 66**,** 262-272.

Zhang, D., He, Q., Wang, M., Zhang, W. & Liang, Y. 2019. Sorption of perfluoroalkylated substances (PFASs) onto granular activated carbon and biochar. *Environmental Technology***,** 1-12.

Zhao, X., Li, J., Shi, Y., Cai, Y., Mou, S. & Jiang, G. 2007. Determination of perfluorinated compounds in wastewater and river water samples by mixed hemimicelle-based solid-phase extraction before liquid chromatography–electrospray tandem mass spectrometry detection. *Journal of Chromatography A,* 1154**,** 52-59.
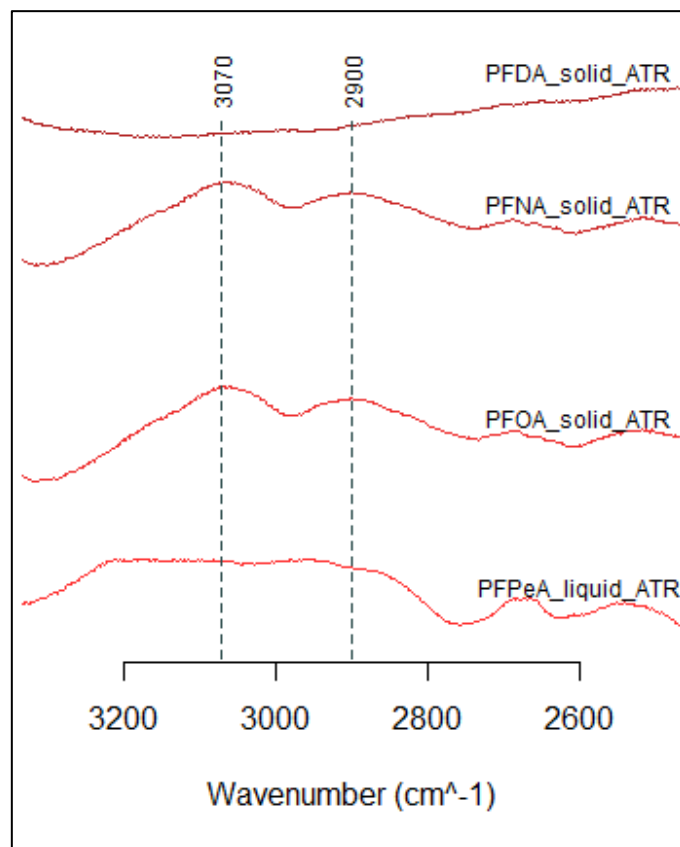
Appendix

Section A: Additional spectra

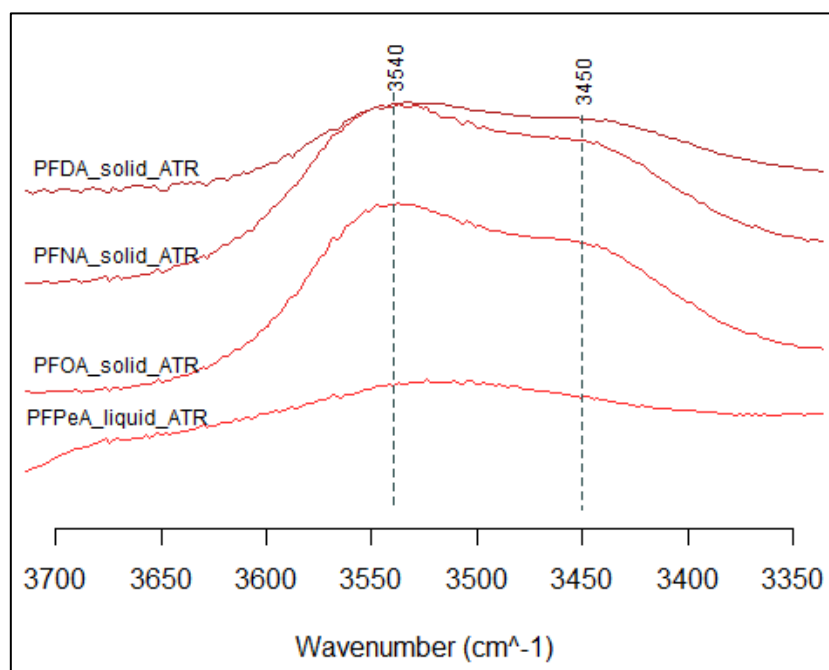Figure A 1: IR spectra of pure PFCAs in 3200 − 2600 cm^{-1} region.

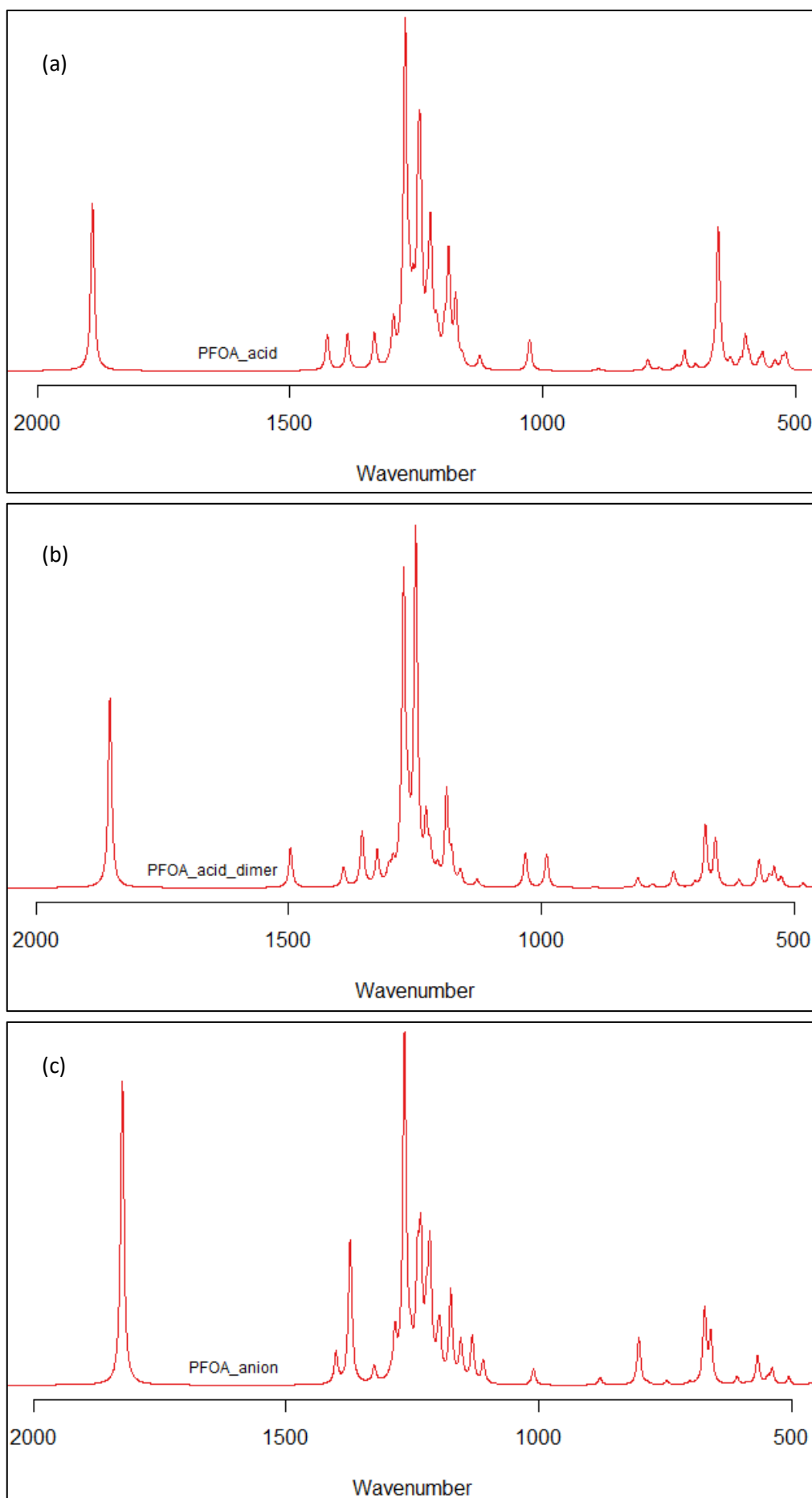Figure A 2: IR spectra of pure PFCAs in 3700 − 3350 cm^{-1} region.

Figure A 3: Theoretical absorbance spectra of the (a) protonated PFOA acid (b) PFOA acid dimer (c) deprotonated PFOA anion.
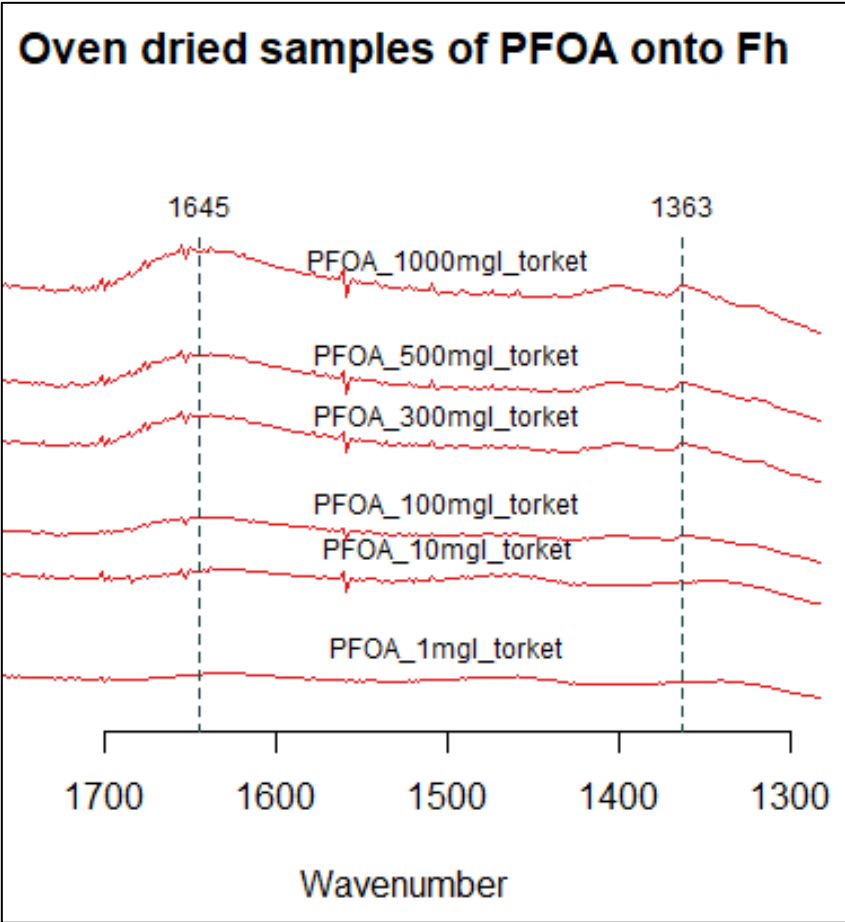
Figure A 4: Carboxylate region (1700 – 1300 cm^{-1}) for the oven dried sorption samples with PFOA.
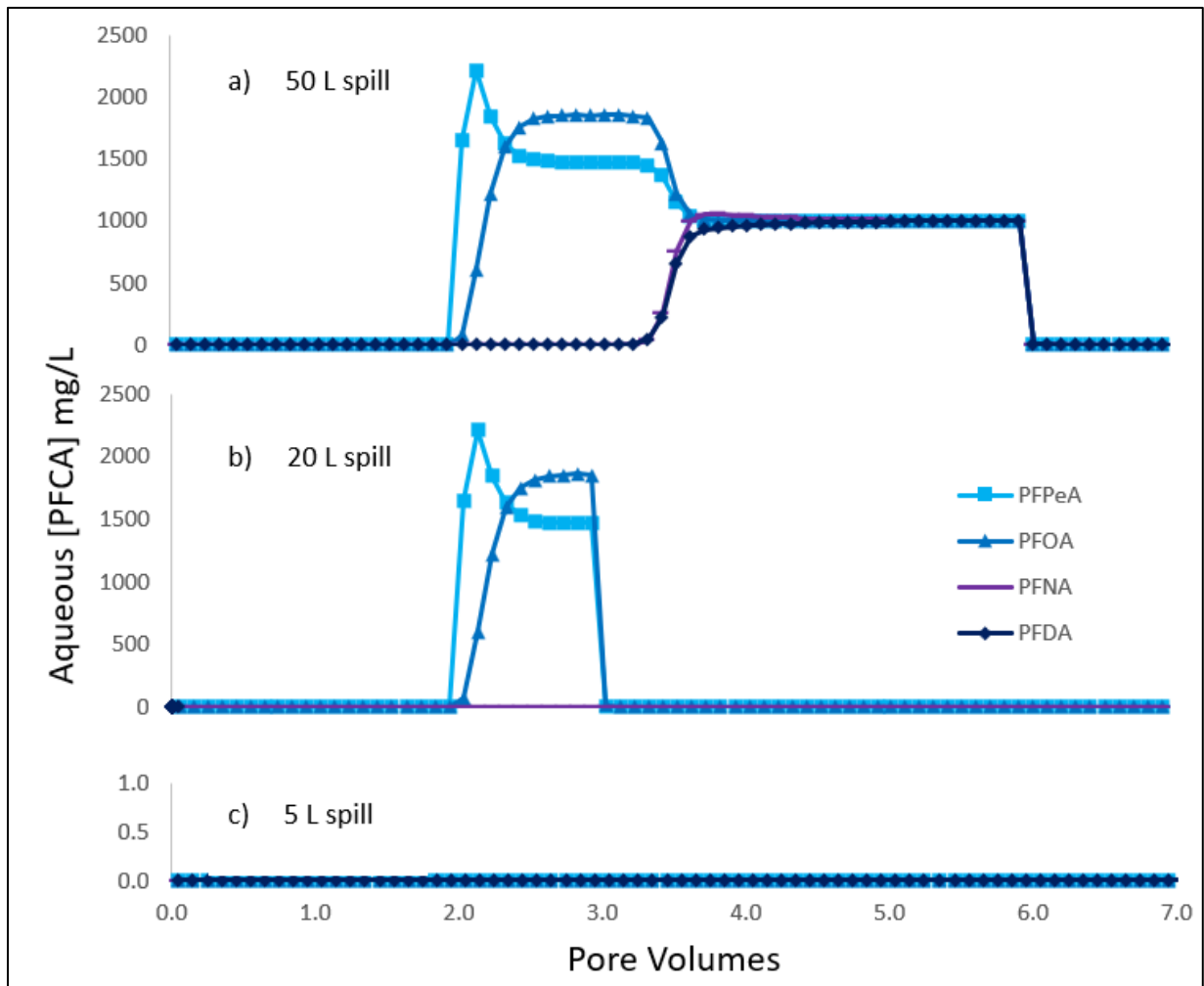
Section B: PHREEQC modeling

Figure B 1: Transport model with different spill scenarios. Aqueous concentrations are measured at 1000 m distance from the contamination source and represent input to a recipient. (a) A 50 L, (b) 20 L and (c) 5 L pulse of contaminated water.
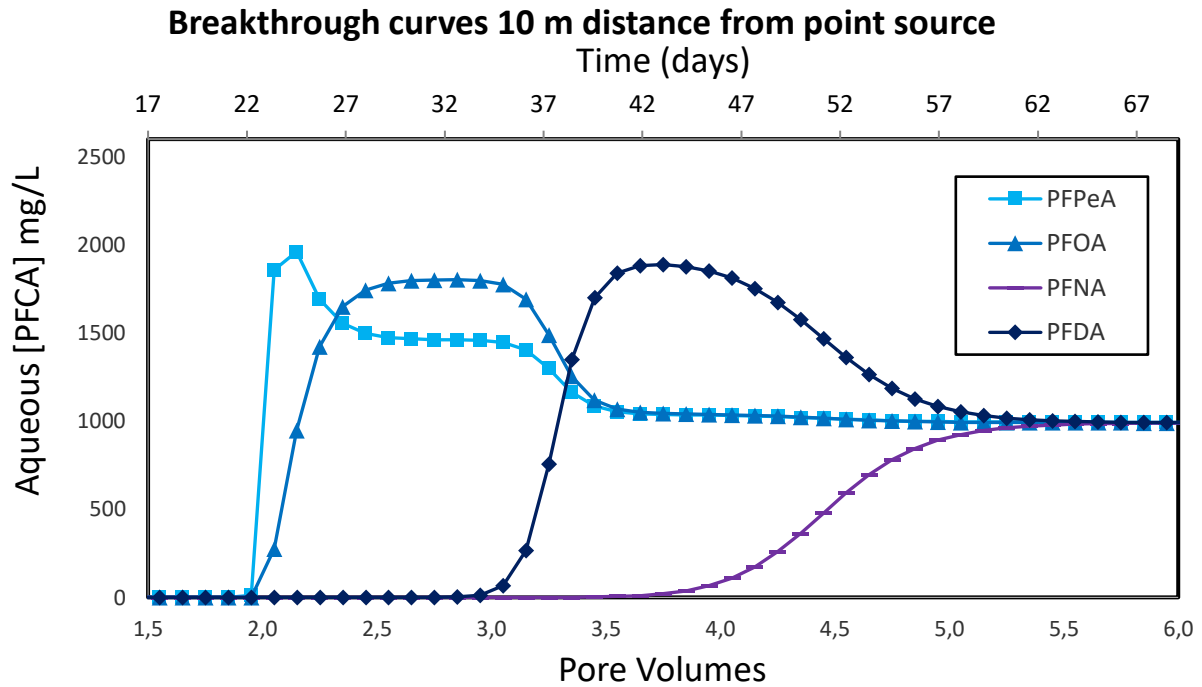
Figure B 2: Transport simulated breakthrough curves using only Freundlich parameters from table 8.

PHREEQC Database blocks for the PFCAs:

```
SOLUTION_MASTER_SPECIES

Pfpea Pfpea-      0 C5F9O2H 264.0459

Pfoa  Pfoa- 0 C8F15O2H 414.0684

Pfna  Pfna- 0 C9F17O2H 464.0759

Pfda  Pfda- 0 C10F19O2H 514.0834

SOLUTION_SPECIES

Pfpea- = Pfpea-

     -log_k      0

Pfoa- = Pfoa-

     -log_k      0

Pfna- = Pfna-

     -log_k      0

Pfda- = Pfda-

     -log_k      0

# pKa from (Steinle-Darling and Reinhard, 2008) were chosen because pKa's

# for PFCAs are not thoroughly determined, and this way
```

```
# almost all acid will dissociate.

Pfpea- + H+ = PfpeaH

      log_k -0.1

Pfoa- + H+ = PfoaH

      log_k -0.2

Pfna- + H+ = PfnaH

      log_k -0.21

Pfda- + H+ = PfdaH

      log_k -0.21

SURFACE_MASTER_SPECIES

      Z              Z+    #2-line Ferrihydrite

SURFACE_SPECIES

      Z+ = Z+

      -log_k 0

#Freundlich sorption

Z+ + 0.3201Pfpea- = PfpeaZ    # Kf*C^n = 5.9364*C^0.3201

      -log_k 0.773523

      -no_check

      -mole_balance PfpeaZ

Z+ + 0.51278Pfoa- = PfoaZ     # Kf*C^n = 8.511144*C^0.51278

      -log_k 0.929988

      -no_check

      -mole_balance PfoaZ

Z+ + 0.8465Pfna- = PfnaZ      # Kf*C^n = 578.75*C^0.8465

      -log_k 2.762491

      -no_check

      -mole_balance PfnaZ

#Linear sorption

Z+ + Pfda- = PfdaZ            # Linear sorption of PFDA is preferred

                             # with initial data

      -log_k 3.053032        # K_Fh = 1129.88

# Alternative sorption isotherm when excluding presumed undissolved data:

# Kf*C^n = 153*C^0.7921
```

PHREEQC input-file for models in figure B 1:

```
SOLUTION 0              #Contaminated water
     units mol/l
     pH    7
     Pfpea 3.787e-3   # 1000 mg/L
     Pfoa  2.415e-3   # 1000 mg/L
     Pfna  2.154e-3   # 1000 mg/L
     Pfda  1.945e-3   # 1000 mg/L
SOLUTION 1-10
     pH    7
COPY solution 0 200
COPY solution 1 201                   # Copying clean water to another
                                      # solution outside the model.

END


USE solution 1
SURFACE 1-10 # Ferrihydrite surface
     -equilibrate 1-10
     Z     0.0115     450   5.8   # The same surface-properties as for
                                  # the models in figure 14 and 15.
END


TRANSPORT 1
     -cells 10
     -shifts 50                 # The amount of shifts determines the pulse
                                # of contaminated water in L.
     -time_step 10000000        # Time per shift, GW-velocity of
                                # 100 m / 10e7 s = 10e-5 m/s.
     -lengths    100            # Length of cell in meters.
     -dispersivities   0
     -diffusion_coefficient 0
     -punch_cells 10
     -punch_frequency 1
COPY solution 201 0              # Changing SOLUTION 0 to clean water.
END


TRANSPORT 2
     -shifts    100             # Pumping clean water after the contamination
                                # pulse.
END
```

Table B 1: Sorption parameters from every batch reaction sample set, including PFOA

PFCA	Freundlich constants		Linear
	K_f	n	K_{Fh}
PFPeA	5.9	0.3201	308
PFOA	8.5	0.5128	183
PFNA	578.8	0.8465	1556
PFDA	142666	1.755	1129.9[a]
PFDA excluding undissolved	153	0.7921	673.3
PFOA dried samples	16.2	0.4096	667
PFOA with Fh at 5 g/l	3254	1.2336	757.3

[a]K_{Fh} value used in the database to generate models for figure 14 and 15.